

<https://doi.org/10.1038/s43247-024-01571-9>

The flotation of magmatic sulfides transfers Cu-Au from magmas to seafloor massive sulfide deposits

Check for updates

Aurélien Jeanvoine ^{1,2} , Jung-Woo Park ², Ewan Pelleter¹, Antoine Bézous³, Gilles Chazot¹, Jiwon Hwang² & Yves Fouquet¹

Copper and gold-rich seafloor massive sulfide deposits formed in intra-oceanic subduction settings are typically associated with hydrous and oxidized magmas, but processes leading to their formation remain controversial. Sulfide-bubble interaction has been suggested to play an important role in metal transfer from magmas to seawater-derived hydrothermal fluids. Here we use textural observations of magmatic sulfides, geochemical numerical models of chalcophile element concentrations, and numerical models of magmatic sulfide growth within a mafic to felsic submarine magmatic suite (Fatu Kapa, SW Pacific) associated with copper-gold-rich seafloor massive sulfide deposits. We demonstrate that concomitant sulfide and aqueous fluid formation at the andesitic stage results in floating sulfide-bubble compound drops in magmas, which play a crucial role in the transfer of copper and gold toward the surface. We emphasize that late sulfide saturation in copper-gold-rich intra-oceanic subduction-derived felsic magmas favors upward sulfide transfer via flotation.

Cu-Au-rich seafloor massive sulfide (SMS) deposits are mostly found in close association with oxidized magmas that formed during intra-oceanic subductions due to the influx of slab-derived aqueous fluids into the mantle wedge¹. The mechanisms by which SMS ores were enriched in chalcophile elements, which have an affinity for both sulfides^{2–4} and aqueous fluids^{5–8} in magmas are currently the focus of intense debate.

Under high magmatic oxygen fugacity (fO_2), soluble sulfate species are more prevalent than less soluble sulfide species⁹. Consequently, sulfide saturation in oxidized intra-oceanic subduction magmas differs from that of more reduced mid-oceanic ridge settings. In the former, sulfide saturation is delayed toward a later differentiation stage and is triggered by factors such as magnetite crystallization^{10–13}, volatile saturation¹⁴ or changes in magmatic composition¹⁵. As a result, during the early S-undersaturated stage of magmatic evolution ($MgO \geq 4$ wt%), the concentration of chalcophile elements such as Cu increase by more than a factor of ~2 in oxidized magmas compared to their Mid-Ocean Ridge Basalt (MORB) counterparts. This process is well displayed by subduction-related magmas like Niuatahi-Motutahi, Valu Fa Ridge, and Pual Ridge (Fig. 1a). Subsequently, Cu concentrations abruptly decrease at MgO contents of ~2–4 wt%. A similar drop in concentration is observed in other chalcophile elements such as Pd and Se, which have a limited affinity for aqueous fluids^{11,13,16,17}. The decrease suggests that these elements are strongly partitioned into dense, immiscible

sulfide melts^{11–13,17,18}. However, water saturation can compete with sulfide partitioning by scavenging chalcophile elements into low-density bubbles of aqueous fluids^{5–8}. This versatile behavior of chalcophile elements, along with the geochemical signatures of magmatic sulfides (e.g., chalcophile element ratios) and magmatic fluids (e.g., high CO_2 concentrations, sulfur isotopic composition) preserved in hydrothermal vents, SMS, and epithermal ores, or subaerial arc volcanic gases^{19–23}, has led to the emergence of two diverging models. These models propose that Cu and Au are transported to the surface either by magma-derived fluids mixed with varying amounts of seawater-derived hydrothermal fluids^{10,12,24,25} or through hydrothermal remobilization of magmatic sulfides^{11,13,25}.

These two models were reconciled in an experimental study²⁶. The study demonstrated that when sulfide blebs and aqueous fluid bubbles exsolve simultaneously, they stick together to form compound drops that can float toward the surface^{26,27}. The dissolution of sulfides by bubble fluid results in sulfur transfer toward aqueous fluids and sulfide consumption, leaving only minor evidence of upward sulfide transfer in natural settings^{26,28–30}. However, it has also been suggested that owing to their small size, magmatic sulfides could be carried upward by ascending magmas without requiring flotation²⁹. Although sulfide-bubble compound drops have been observed in natural magmas, these are typically trapped within^{19,31} or between^{28,32–38} phenocrysts. This leads to bubble flattening^{28,37},

¹UMR6538 Geo-Ocean, IFREMER CNRS UBO UBS, Plouzané, France. ²School of Earth and Environmental Science, Seoul National University, Seoul, Republic of Korea. ³Nantes Université, Univ Angers, Le Mans Université, CNRS, Laboratoire de Planétologie et Géosciences, Nantes, France.

e-mail: aurelien.jeanvoine@gmail.com

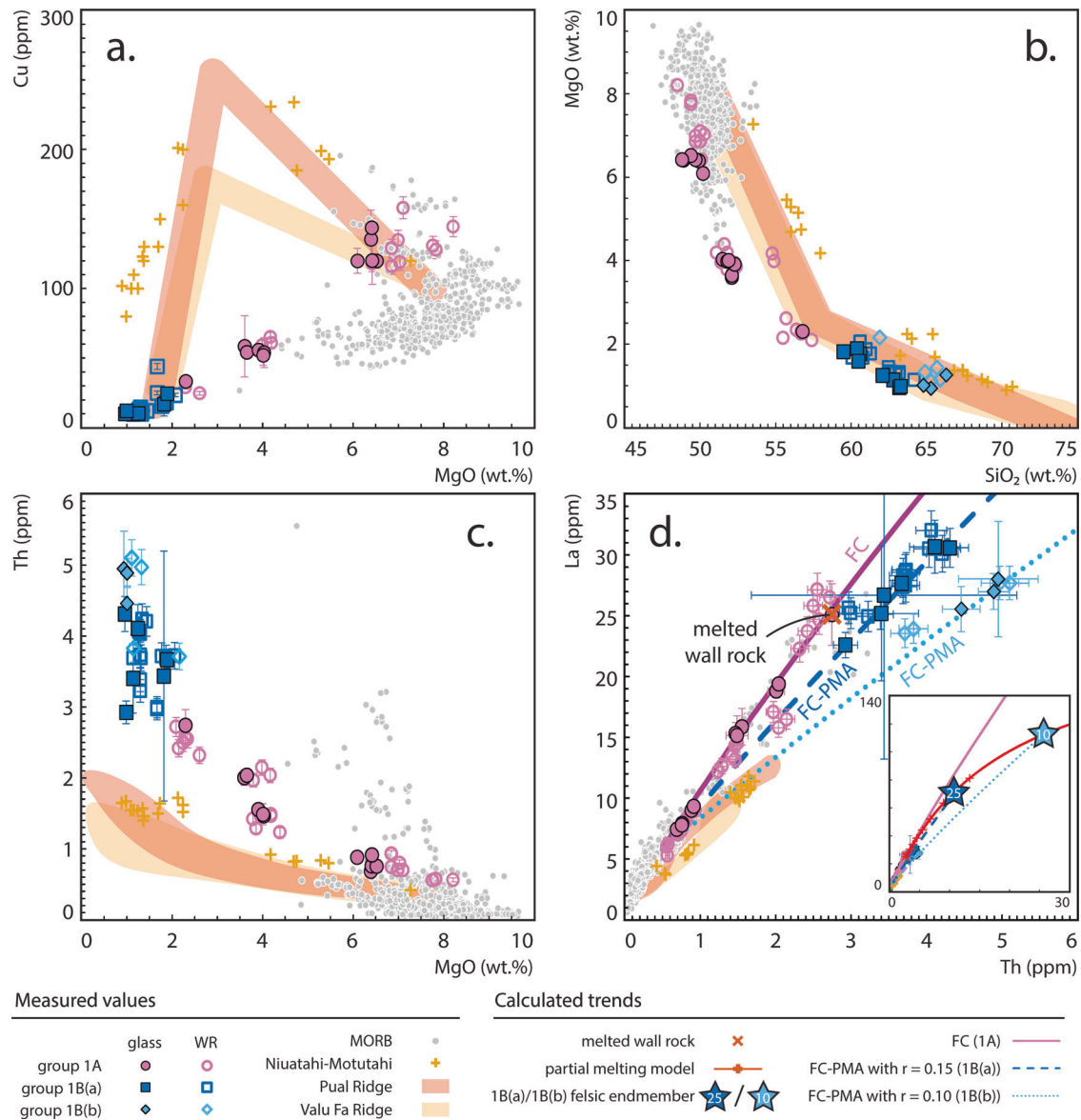


Fig. 1 | Geochemistry of Fatu Kapa lavas compared to mid-ocean ridge basalts and intra-oceanic lavas. Cu versus MgO (a), MgO versus SiO₂ (b), Th versus MgO (c), and La versus Th (d) for Fatu Kapa whole rocks (WR, open circles) and glasses (filled circles) in groups 1A (purple color), 1B(a) and 1B(b) (dark and light blue, respectively). The uncertainties for Cu, Th, and La are 5% of the measured value for whole rocks, and for glass measurements they are provided at a 2-sigma level. Whilst group 1A magmas align well with a Fractional Crystallization (FC) model in (d) (purple trend labeled FC), groups 1B(a) and 1B(b) magmas evolve through more

complex Fractional Crystallization-Partial Melting Assimilation models (dark and light blue trends labeled FC-PMA in panel d)³⁹, see Methods for more details. Inset in (d): red curve, calculated partial melts of local altered oceanic crust; dark blue star: 25% partial melting; light blue star: 10% partial melting; dark and light blue curves are FC-PMA models. Data for Mid-Ocean Ridge Basalts (MORB)⁷⁶, and the subduction-related magmas of Niuatahi-Motutahi¹², Pual Ridge¹¹, and Valu Fa Ridge¹³ are reported for comparison (see legend insert for symbols list).

shrinking^{19,31}, and/or infilling with late-stage silicate liquid^{28,32-38}, posing challenges in estimating the densities of compound drops essential for determining whether flotation is required to carry sulfides upward.

Cu and Au-rich SMS ores (Supplementary Note 1; Supplementary Fig. 1) have been identified in the Fatu Kapa area (NW Lau back-arc basin, SW Pacific) in close association with reduced magmas (Supplementary Fig. 2) that exhibit a sub-alkaline trend. These magmas are subdivided into two groups: group 1A magmas evolve from basaltic to trachy-andesitic compositions by fractional crystallization, while shallower group 1B magmas evolve from a primary magma akin to the group 1A basalt toward dacitic compositions by fractional crystallization coupled with assimilation of a felsic endmember (Fig. 1b, c, d; Table 1)³⁹. This endmember is generated by

partial melting of the local hydrothermally altered crust, with 1B(a) (this paper) and 1B(b) (not examined here) magmas generated by a partial melting degree of 25% and 10%, respectively. In this study, we investigate the transfer of metals from Fatu Kapa magmas to the surface by floating sulfides. To achieve this, we examine the textural relationship between sulfides and aqueous fluid bubbles within Fatu Kapa magmas. We also examine the onset of sulfide blebs and pre-eruptive bubbles formation using geochemical models focused on chalcophile elements (Cu, Pd, Zn, and Pb). We propose a model of sulfide growth to test whether sulfide flotation is necessary for the physical transfer of magmatic sulfides. Finally, we discuss the role of compound drops in carrying metals from initially oxidized slab-coupled magmas.

Table 1 | Composition in major elements and estimated water concentrations of lavas representative of the Fatu Kapa sub-alkaline suite

	Basalt (1A and 1B(a))	Andesite (1B(a))	Dacite (1B(a))
Sample	FU2-DR26-02	FU3-DR13-05 (1A) + H ₂ O	FU3-PL03-03
SiO ₂ (wt%)	49.69	56.80	63.30
Al ₂ O ₃ (wt%)	14.84	14.30	13.31
MgO (wt%)	6.99	2.30	0.99
CaO (wt%)	11.99	5.58	3.25
FeO _{tot} (wt%)	11.54	11.10	7.16
TiO ₂ (wt%)	1.65	1.79	1.02
Na ₂ O (wt%)	2.82	4.20	5.95
K ₂ O (wt%)	0.49	1.32	2.06
Total without H ₂ O (wt%)	100.17	97.37	97.04
Estimated H ₂ O (wt%)	0.40	2.10	2.10
T (°C)	1160–1180	1070	980–1020
log(η) (Pa.s)	1.45	2.97	3.51
Lava texture	Fine-grained matrix, few (<5%) phenocrysts	Fine-grained matrix, few (~15%) phenocrysts	Mostly aphyric
Sinking velocity of isolated sulfides after ~1 year (m year ⁻¹) (log unit)	2.00	1.18	0.30
Ascending velocity of simple compound drops (m year ⁻¹) (log unit)	-	0.17	-1.04
Ascending velocity of multiple compound drops (m year ⁻¹) (log unit)	-	1.62	0.78

Temperatures, viscosities (η)⁶⁸ and sinking sulfide velocities as well as ascending compound drops velocities are indicated. Andesites were not measured in group 1B(a). Instead, we estimated their potential composition using a volatile-saturated group 1A andesite with a water content equivalent to the water solubility of group 1B(a). The sinking velocities are those at ~1 year after sulfide formation, when the sulfide radius increases at a slower pace. See “Transfer of Cu and Au from Fatu Kapa magmas to the surface” for details.

Results and discussion

Magmatic sulfides

We observed a total of 42 sulfide blebs in group 1A magmas (basalt-andesites) (Supplementary Figs. 3–7). Only 10 of these sulfides are associated with bubbles (Fig. 2a). Sulfide blebs are generally small, with a diameter typically below 15 μm , but larger sulfides may reach up to 65 μm . Individual sulfides are predominantly composed of pyrrhotite, which forms upon exsolution of monosulfide solid solutions (MSS) that crystallized from Fe-S sulfide liquids. These pyrrhotites exhibit micrometric unconnected pores that occupy ~10–20% of the bleb volume. Within these sulfide blebs, inframetric to micrometric Cu-rich phases are identified. These Cu-rich phases occupy about 5–15% of the bleb volume and are typically located near MSS pores. In addition to the sulfide blebs, there are fewer elongated sulfides and sulfide impregnations, which correspond to burst sulfide blebs.

We observed 55 sulfide blebs in group 1B(a) magmas (Supplementary Figs. 3, 4), 48 of which are connected to a larger bubble that can range in diameter from 20 μm up to several hundreds of μm (Fig. 2b). Most of the sulfide blebs observed in magmas of dacitic composition exhibit a similar diameter to those of group 1A (i.e., <15 μm). Individual sulfides also display similar chemistry and textures to those of group 1A.

The presence of aqueous fluid in the form of bubbles has a notable impact on the texture and composition of associated sulfides. Firstly, sulfides attached to bubbles exhibit numerous holes with radii increasing from nanometric scale up to 1 micrometer as they approach the bubble interface (Fig. 2a, b). Some of the holes are interconnected to the proximity of the bubble, suggesting sulfide dissolution by the aqueous fluid. Secondly, micrometric Cu-rich phases are frequently observed in the section of the sulfide bleb located near the bubble interface (Fig. 2b). These phases likely formed due to an increase in metal content resulting from sulfur degassing into the fluid, as supported by experimental evidence³⁰. Finally, several sulfides associated with a bubble identified in group 1A exhibit various stages of oxidation, ranging from a slight replacement by oxides along their

borders to complete oxidation (Fig. 3a, b, c). During this process, most of the MSS pores become partially to fully filled with iron oxides (Fig. 3a). Only three of the 55 sulfides observed in group 1B(a) display evidence of oxidation alongside dissolution (Fig. 3d).

When observed in thin sections, sulfide bleb-bubble interfaces sometimes consist of small thin sulfides growing from the primary sulfide toward the vesicle cavity (Fig. 3d). This indicates that the secondary sulfides formed through the precipitation of sulfur, previously partitioned into the bubble fluid phase. Up to 16 round-shaped and texturally angular sulfides were observed (Fig. 2c, d) on several bubble rims of 1B(a) magmas. These sulfides represent the same sulfide-bubble interface and, therefore, conceal the primary sulfide on which they were deposited. Conversely, identification of these large bubbles punctuated by multiple round and angular sulfides, whose sizes are similar to the primary sulfides observed in cross-section (e.g., white box in Fig. 2d), suggests that numerous sulfide blebs are associated with these bubbles. The existence of these multiple compound drops has been firmly identified in an experimental study³⁰, and decorated vesicles previously interpreted as the result of sulfide condensation in ridge basalts^{40,41} may correspond to multiple compound drops similar to those identified in our study. This suggests that the sulfide-bubble association may be common in natural settings. A semi-quantitative analysis of the deposited sulfides using scanning electron microscopy revealed that a substantial proportion are Cu-rich. This attests that bubbles formed at the felsic stage contain substantial amounts of Cu.

Water content and volatile saturation

We estimated water content in group 1 magmas using a temperature-dependent plagioclase-silicate melt hygrometer⁴² and iteratively integrated temperatures with a plagioclase-silicate melt thermometer⁴³ (Supplementary Notes 2, 3; Supplementary Figs. 8, 9; Supplementary Table 1). The hygrometer has a standard estimated error of 0.35 wt%⁴². Group 1A magmas have less than 1 wt% H₂O, while group 1B(a) felsic magmas contain 1.2–2.2 wt% H₂O (Fig. 4a).

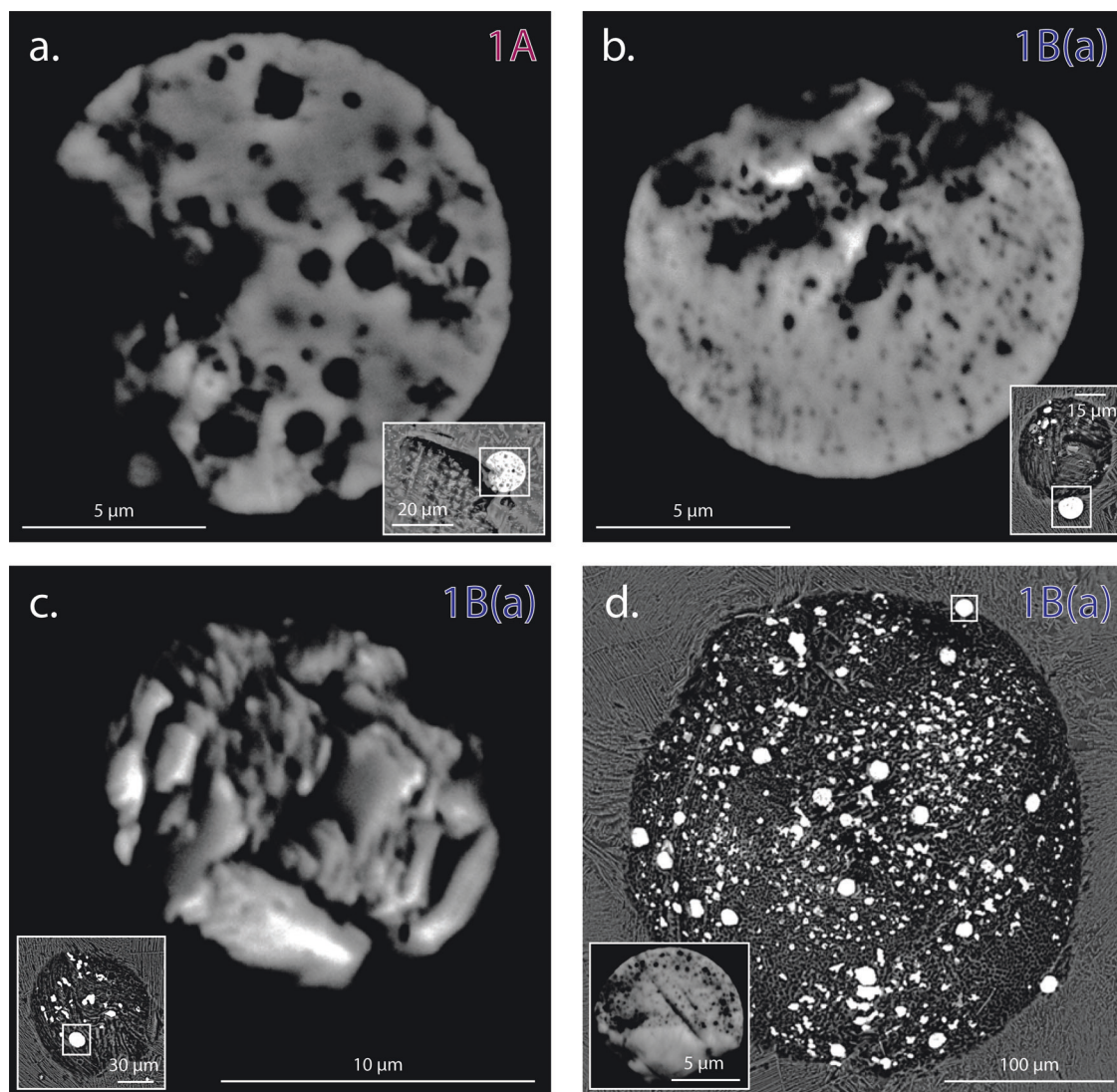


Fig. 2 | Scanning electron microscope (SEM) images of sulfide blebs associated with bubbles. **a** Sulfide bleb linked to a deformed bubble in the silicate melt of a group 1A lava (sample FU3-DR-01-10, sulfide p194). **b** Sulfide bleb linked to a bubble within the silicate liquid of a group 1B(a) lava (sample FU2-DR-27-05, sulfide p159). Note the presence of Cu-rich phases (white areas) near the bubble and the increasing pore size near the bubble. **c** View of the sulfide-bubble interface from inside the bubble in a group 1B(a) lava (sample FU2-DR-27-05, sulfide p24). The main image is looking into the curved inner surface of the bubble. Note the round shape, angular, and massive texture of sulfides. Some areas with high Cu concentrations are recorded. **d** Bubble linked to a single sulfide in the plan view of the

thin section (white box) of a group 1B(a) lava (sample FU2-DR-27-05, sulfide p123). Inset of **(d)** shows that the sulfide bleb texture is different within the silicate melt (porous texture and perfect circular shape) than inside the bubble (massive texture with irregular and pseudo-angular shapes similar to the example shown in **(c)**). Note the presence of other round-shaped sulfides inside the bubble, similar in diameter to the sulfide observed in the thin section plan view (white box). These sulfides represent the sulfide-bubble interface deposited on primary sulfides, suggesting that this bubble is linked to multiple magmatic sulfides. White boxes indicate the location of the zoomed area in the main picture (**a**, **b**, **c**), or in the inset (**d**).

Aqueous fluids separated from volatile-saturated magmas primarily consist of H₂O and CO₂, but experiments conducted in volatile-saturated magmas have shown that the fluid phase is dominated by H₂O for pressures below 2.5 kbar²⁶. Group 1A magmas yield a relatively constant pressure of 2.8 ± 1.7 kbar ($n = 42$, $\sim 10.4 \pm 6.4$ km), while group 1B(a) magmas yield a pressure of 0.5 ± 0.6 kbar ($n = 13$, $\sim 1.9 \pm 2.2$ km) (Fig. 4b). Therefore, we have not considered the behavior of CO₂ and assumed that a water-rich fluid phase is formed when the H₂O content of the magma reaches its water solubility. We estimated the pressure evolution as a function of water solubility for both basaltic and rhyolitic magmas using VolatileCalc⁴⁴ (Fig. 4b). Group 1A magmas exhibit maximum water concentrations of 0.95 ± 0.35 wt% which are five times lower than the water solubility of basaltic magmas at the estimated average magmatic pressure. In contrast, dacitic magmas from group 1B(a) have water concentrations ranging from 1.2 to 2.2 wt%, and these concentrations intersect, within uncertainties, the

water solubility curve of rhyolitic magmas at the estimated magmatic pressures. Consequently, group 1A magmas remain volatile-undersaturated before eruption throughout their evolution, while the felsic magmas of group 1B(a) are more likely to be in equilibrium with an aqueous fluid phase.

Chalcophile elements and sulfide saturation

The most mafic magmas within group 1A show enrichment in Highly Chalcophile Elements (HCE, Cu, and Pd) compared to MORB at similar Th concentrations (Fig. 5), used as a proxy of magmatic differentiation. Their behavior during magmatic evolution is often used to pinpoint the onset of sulfide saturation. Indeed, HCE are highly compatible with sulfide liquids, with Pd having a stronger affinity compared to Cu^{2,12,18,45,46}. From the most mafic sample of group 1A up to a Th value of ~ 0.70 ppm, both Cu and Pd contents increase as Th increases, while the Pd/Cu ratio remains constant.

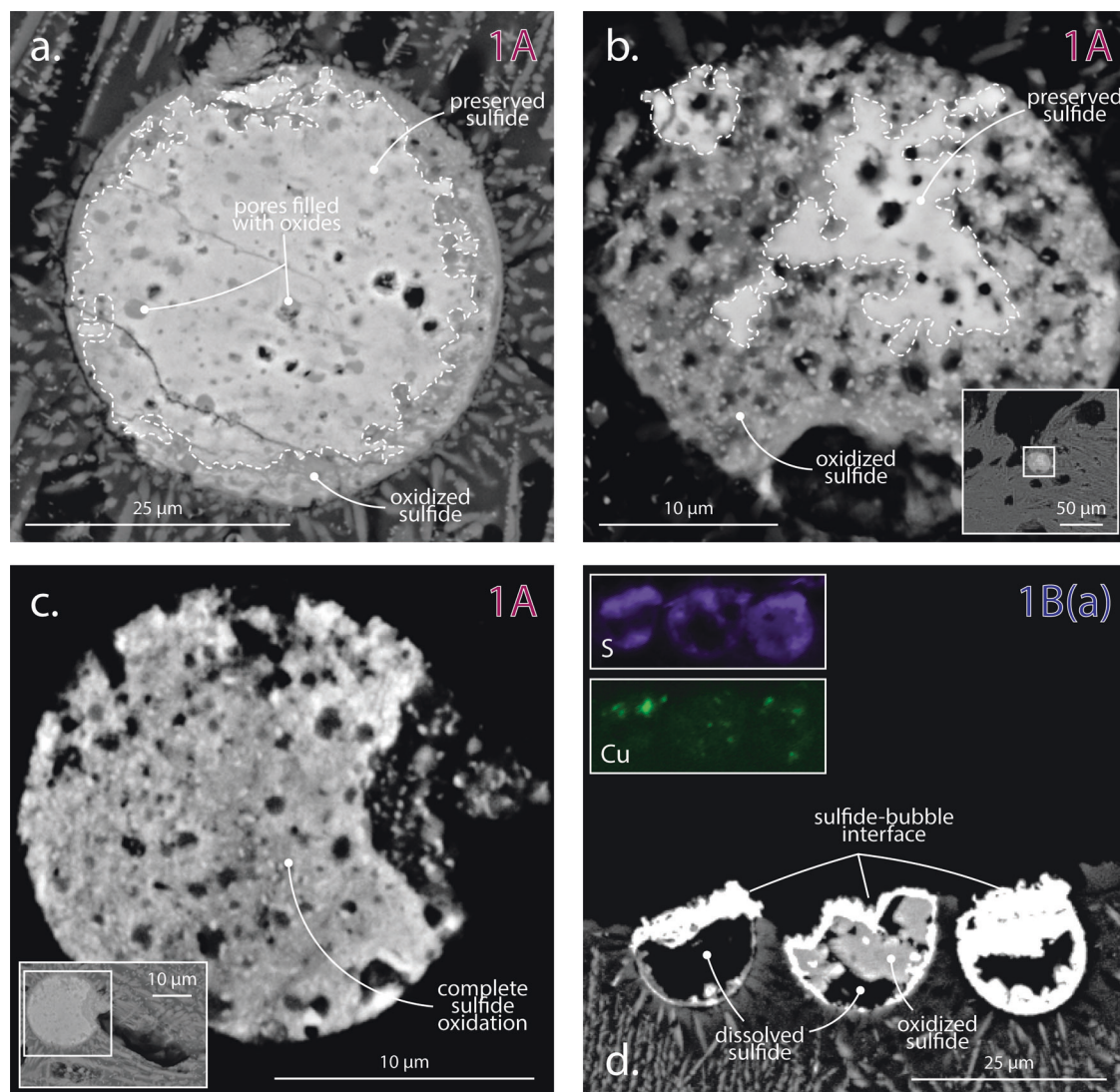


Fig. 3 | SEM images of oxidized sulfide blebs. a Sulfide displaying slightly oxidized borders with most pores showing slight to full coating with oxides (group 1A, sample FU3-DR-01-10, sulfide p44). **b** Considerably oxidized sulfide linked to a bubble (group 1A, sample FU3-DR-01-10, sulfide p119). **c** Fully oxidized sulfide associated with a deformed bubble (group 1A, sample FU3-DR-01-10, sulfide p175). **A**

chemical map of this sulfide is available in Supplementary Fig. 7. **d** Three sulfides with varying degrees of dissolution and/or oxidation attached to the same bubble (group 1B(a), sample FU2-DR-27-05, sulfide p17). S and Cu chemical maps are shown in the insets.

This indicates an initial stage of evolution under S-undersaturated conditions (Fig. 5a, b, c). Beyond ~ 0.70 ppm Th, both Cu and Pd decrease as Th increases, and the Pd/Cu ratio also decreases, indicating that sulfide saturation is reached. It is worth noting that Pd replicate analyses are similar within uncertainty below ~ 0.70 ppm Th, whereas they are less reproducible in more evolved samples (Th > 1 ppm, Fig. 5b). We attribute this poor reproducibility to the uneven distribution of sulfide liquid droplets in S-saturated magmas, which is consistent with previous studies^{12,18,46}. Moreover, Pd content experiences a considerable drop once sulfide saturation is reached, followed by a less pronounced decrease with increasing Th (Fig. 5b). This suggests a change in the nature of the segregated sulfide phase, for which Pd affinity is less pronounced. Moderately chalcophile element (Zn and Pb) concentrations measured in the most mafic magmas within group 1A are similar to those observed in MORB. Notably, the Zn and Pb contents in group 1A magmas increase with increasing Th values before and after sulfide saturation because these elements are substantially less compatible with sulfides compared to HCE⁴⁷.

In group 1B(a) magmas, Pd concentrations vary considerably, differing by more than one order of magnitude from one lava to another, for a similar Th content (Fig. 5b). We attribute these variations to the sampling of different batches of magmas originating from the same reservoir in which sulfides are unevenly distributed. However, despite the differences between the lava flows, the replicated sample analyses exhibit limited discrepancies, which are lower than one order of magnitude. This suggests that sulfides are distributed relatively homogeneously at the sample scale. Given the narrow range in Th concentrations for group 1B(a), the lowest Pd concentration measured in these lavas represents the maximum Pd concentration of silicate liquids, indicating the presence of fewer sulfide liquid droplets compared to the other samples (Fig. 5b). This concentration is approximately two orders of magnitude lower than the mafic endmember. The Cu content of group 1B(a) magmas is also lower than the mafic endmember with values ranging from 10 to 25 ppm. This suggests that these magmas reached sulfide saturation during their evolution before the felsic stage. Moderately chalcophile elements exhibit similar behavior to rare earth elements (REE) (Figs. 1 and 5d, e; Supplementary Fig. 10). This suggests that their evolution

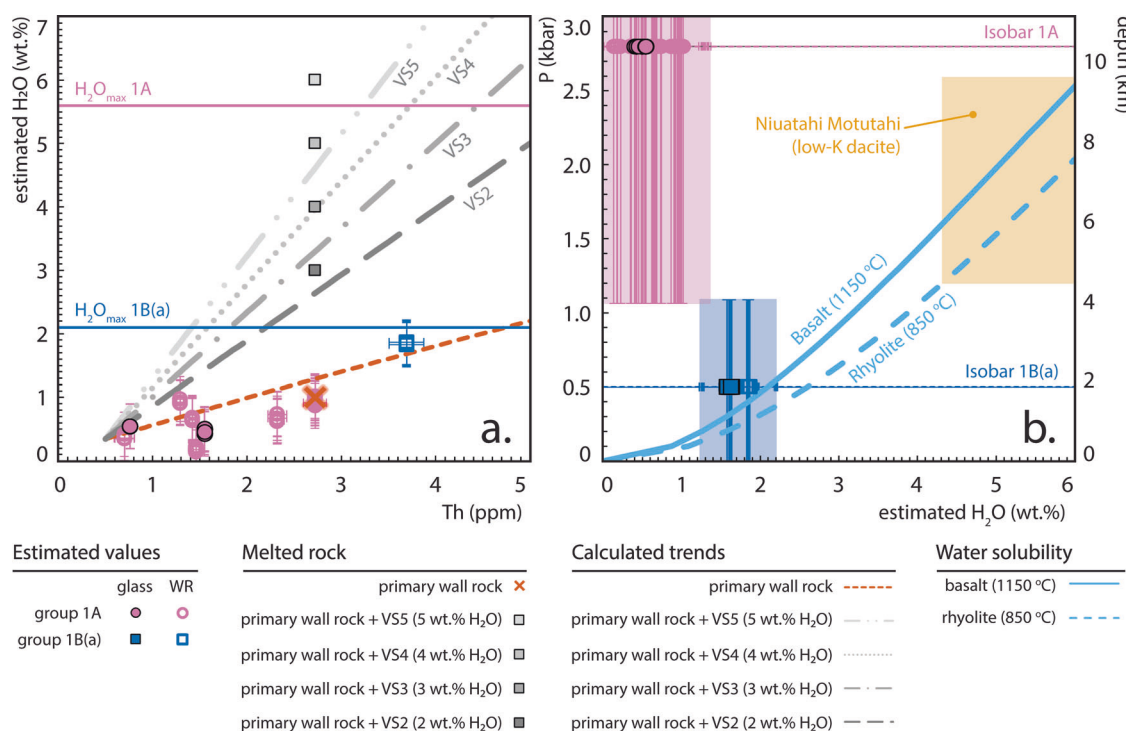


Fig. 4 | Water saturation in Fatu Kapa magmas. **a** Estimated water content (wt%) of group 1A and 1B(a) whole rocks and glasses as a function of their Th content (ppm). The uncertainty for the estimated water content is the standard estimated error of the hygrometer (0.35 wt%)⁴². The uncertainty for Th is the same as in Fig. 1. H₂O_{max} refers to the water solubility at 2.8 kbar for group 1A (purple horizontal line) and at 0.5 kbar for group 1B(a) (blue horizontal line). Shaded gray lines labeled VS5, VS4, VS3, and VS2 refer to fractional crystallization of a mafic magma from group 1A (low Th and water content) coupled with assimilation of a felsic magma generated by partial melting of the local altered oceanic crust (FC-PMA models, see Methods). Assumed water content levels for melted wall rock are 5, 4, 3, and 2 wt% added to the primary concentration (1 wt%) for VS5, VS4, VS3, and VS2, respectively.

b Estimated pressures of Fatu Kapa magmas as a function of the estimated water contents. Purple and blue areas: estimated pressure and H₂O content uncertainties expressed as one standard deviation for pressure, for groups 1A and 1B(a), respectively. Purple and blue dotted lines represent the median estimated pressures for group 1A and group 1B(a) magmas, respectively. Solid and dashed light blue lines show water solubility curves for basaltic (1150 °C) and rhyolitic (850 °C) magmas calculated using VolatileCalc⁴⁴. The P-H₂O area of the volatile-saturated low-K dacites from the Niuatahi-Motutahi volcano¹³ is indicated in orange (see Implications for details).

is primarily controlled by the same mixing process affecting REE concentrations (Fig. 1d)³⁹.

Evolution of Cu, Pd and Au in Fatu Kapa magmas

We modeled the fractional crystallization paths of chalcophile elements in group 1A magmas using a mafic composition representative of this group of samples (Methods). For Th concentrations lower than 0.70 ppm, the S-undersaturated model align well with the data showing concurrent increases of Th and HCE (Fig. 5a, b). When projected toward lower Th contents, group 1A calculated paths intersect with the MORB field (Fig. 5a, b). Therefore, it is conceivable that group 1A magmas evolved first through S-undersaturated conditions, starting from MORB-like HCE concentrations. This initial evolution would allow Cu and Pd concentrations to increase by approximately a factor of two when they reach Th contents of ~0.70 ppm (MgO content of ~7 wt%, Fig. 1a). Throughout this process, the residual melt fraction decreases from 1.0 to 0.7.

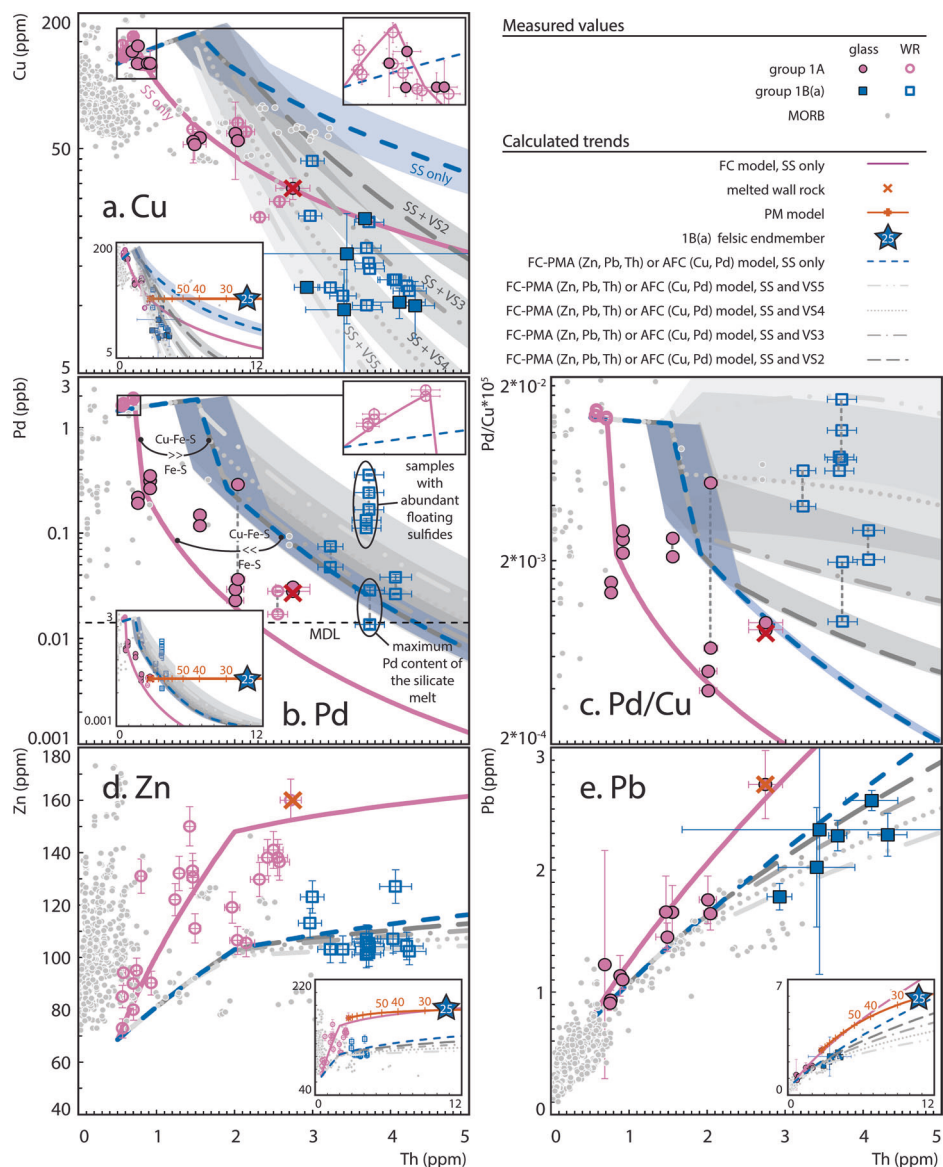
In contrast to some subduction-related magmas, group 1A magmas reach sulfur saturation before the onset of magnetite crystallization, which occurs in the Fatu Kapa magmatic suite at ~2 ppm Th (~4 wt% MgO, Figs. 1a and 5a, b)³⁹. Basaltic magmas from group 1A exhibit MORB-like *f*O₂ that are ~0.5-unit log below the Fayalite-Quartz-Magnetite (FMQ) buffer (Supplementary Fig. 2). Under such reduced conditions, sulfide saturation is expected to occur as early as in MORB, around 9.5 wt% MgO⁴⁶. However, as demonstrated by Cu and Pd data, sulfide saturation in group 1A magmas is delayed to MgO content of ~7 wt%. Sulfide saturation decreases with increasing pressure⁴⁸. The Fatu Kapa area, influenced by the Samoan hot-spot, likely undergoes partial melting at greater depths than MORB³⁹. Thus,

we propose that the initial S-undersaturated stage is due to this greater depth of partial melting (Fig. 6a, b).

Due to this initial S-undersaturated stage of evolution, sulfide saturation in group 1A occurs in Cu-rich (~150 ppm) magmas, which is followed by a drastic drop in Cu and Pd concentrations. Experimental evidence supports that Cu-rich (>100 ppm) magmas form sulfides in the Cu-Fe-S system rather than in the Fe-S system^{4,49}. For instance, magmas from La Fossa (Italy) are Cu-rich (~250 ppm) when they hit sulfur saturation, and Cu-rich (34–66 wt%) sulfides are identified in lavas that encompass Pd and Cu drastic decrease^{50,51}. Although no sulfide blebs were visually observed in group 1A lavas during the Pd-Cu drop, we emphasize that the high apparent compatibility of these elements attests that the segregated sulfides form in the Cu-Fe-S system. Indeed, this drop is well-reproduced by a model for which 0.2 wt% sulfides are formed with Cu-Fe-S:Fe-S proportions of 85:15 (purple curves in Fig. 5). These amounts and proportions align well with those proposed in Cu-rich intra-oceanic arc magmas^{4,50,51}. When the Cu concentration of these magmas decrease below ~100 ppm, the more gradual decrease in Cu and Pd can be accounted for by the formation of sulfides formed in the Fe-S system, in agreement with our petrographic observations (Fig. 2, Supplementary Figs. 3–6).

To account for the compatible behavior of HCE in group 1B(a) magmas, we combined the partial melting of the locally altered crust-mixing model³⁹ with fractional crystallization models. We used the Assimilation-Fractional Crystallization (AFC) model⁵² for HCE and the Fractional Crystallization-Partial Melting and Assimilation (FC-PMA) model for other elements (Methods). The initial mafic magma from the group 1A model served as the starting composition for the group 1B(a) model.

Fig. 5 | Variations in chalcophile element concentrations plotted versus Th. Cu (a), Pd (b), Pd/Cu ratio (c), Zn (d), and Pb (e) versus Th for Fatu Kapa (this study) and MORB magmas⁶. Dashed black dotted horizontal line: Method Detection Limit (MDL) for Pd defined as one standard deviation of the procedural blank. Vertical dotted lines connect the replicate Pd analyses. AFC assimilation coupled with fractional crystallization, SS sulfide saturation, VS volatile saturation. The other acronyms and symbols match those in Fig. 1, with the number above the red partial melting curves referring to the degree of partial melting (%). The uncertainties for Cu, Zn, Pb and Th are the same as in Fig. 1. Those for Pd measurements are provided at a 2-sigma level and fall within the size of the dot. The purple and blue/gray trends depict the modeled evolution of chalcophile elements in group 1A and group 1B(a), respectively. The concentrations measured in group 1A closely match an FC model in which sulfide saturation occurs when the remaining melt reaches about 70% of its initial volume. The blue trends represent models of 1B(a) evolution under volatile-undersaturated conditions, while the gray trends correspond to models VS5, VS4, VS3, and VS2. In these models, sulfide saturation occurs when the remaining melt reaches 70% of its initial volume, mirroring the observation in group 1A. This remaining melt volume is provided with a 10% uncertainty, which is depicted by the sheaths enveloping the 1B(a) trends. Group 1B(a) concentrations align well with the VS2 and VS3 models, for which sulfide and volatile saturation are concomitant. Refer to Methods for additional details.



Similarly with 1A magmas, we triggered sulfide saturation in 1B(a) magmas when the residual melt fraction reaches $0.7 \pm 10\%$ (Methods).

Beyond sulfide saturation, we considered the formation of ~0.2 wt% of a sulfide phase, primarily in the Cu-Fe-S system, followed by the same amount in the Fe-S system. Cu-rich sulfides were not observed, while pyrrhotitic sulfides were identified in dacitic lavas. This model successfully matches measured Pd concentrations (blue line in Fig. 5) but overestimates Cu, Pb, and Zn contents in evolved magmas ($Th > 3$ ppm). This discrepancy may be attributed to the formation of a H₂O-rich volatile phase in 1B(a) magmas, as Cu, Pb, and Zn have an affinity for aqueous fluids⁵⁻⁸.

We have shown that 1B(a) dacitic magmas are saturated with a water-rich fluid phase (Fig. 4). However, the calculated FC-PMA model curve for water is substantially below the water saturation curve (red dotted line in Fig. 4), suggesting that the estimated water content of the endmember is underestimated. It is important to acknowledge that the wall rock in question is hydrothermally altered³⁹ and is likely richer in water than its estimated original composition of ~1 wt%. Since we did not directly sample this altered wall rock, we propose to explore four different scenarios, referred to as VS5, VS4, VS3, and VS2, in which we ascribed 5 wt%, 4 wt%, 3 wt%, and 2 wt% of H₂O to the altered wall rock, respectively. First, we applied our FC-PMA model to each of these scenarios and determined, for each one, the

Th value at which volatile saturation occurs, as well as the amount of fluid formed once the measured compositions of 1B(a) magmas are reached (gray lines in Fig. 4) (see Methods). Secondly, we incorporated these four scenarios into both the AFC and FC-PMA models applied to chalcophile elements (gray lines in Fig. 5). As a result, we found that the measured Cu, Zn, and Pb concentrations in group 1B(a) magmas can be reproduced by the VS4 and VS3 scenarios for which 3.3 wt% and 2.4 wt% of aqueous fluids, respectively, are formed at the andesitic stage.

Transfer of Cu and Au from Fatu Kapa magmas to the surface

The results of our modeling approach suggest that the complex evolution of the Fatu Kapa magmatic system comprises stages during which Cu, and presumably Au, are stored at depth within the crust, and stages during which they are transferred to the surface. We did not measure Au but, similarly with previous studies^{45,53,54}, we rely on the fact that the affinity of this element for sulfides falls between that of Cu and Pd²⁻⁴ to extrapolate its behavior when discussing its contribution.

Throughout most of their evolution, group 1A magmas segregated sulfides and remained undersaturated with respect to volatiles. Accordingly, only a few compound droplets were observed in these samples (inset in Fig. 7a). We computed the evolution of the sulfide radius and sinking

velocity of isolated sulfides in the basaltic magmas of group 1A using a model of sulfide growth by sulfur diffusion and sulfide convection⁵⁵ (see Methods). Isolated sulfide blebs reach a size of 150–200 μm and a sinking

velocity of ~100 m year⁻¹ within less than 1 year (Fig. 7b, c). Therefore, the small, isolated sulfide blebs (<20 μm) identified within group 1A lavas are those that formed shortly before eruption and were entrained by magmas,

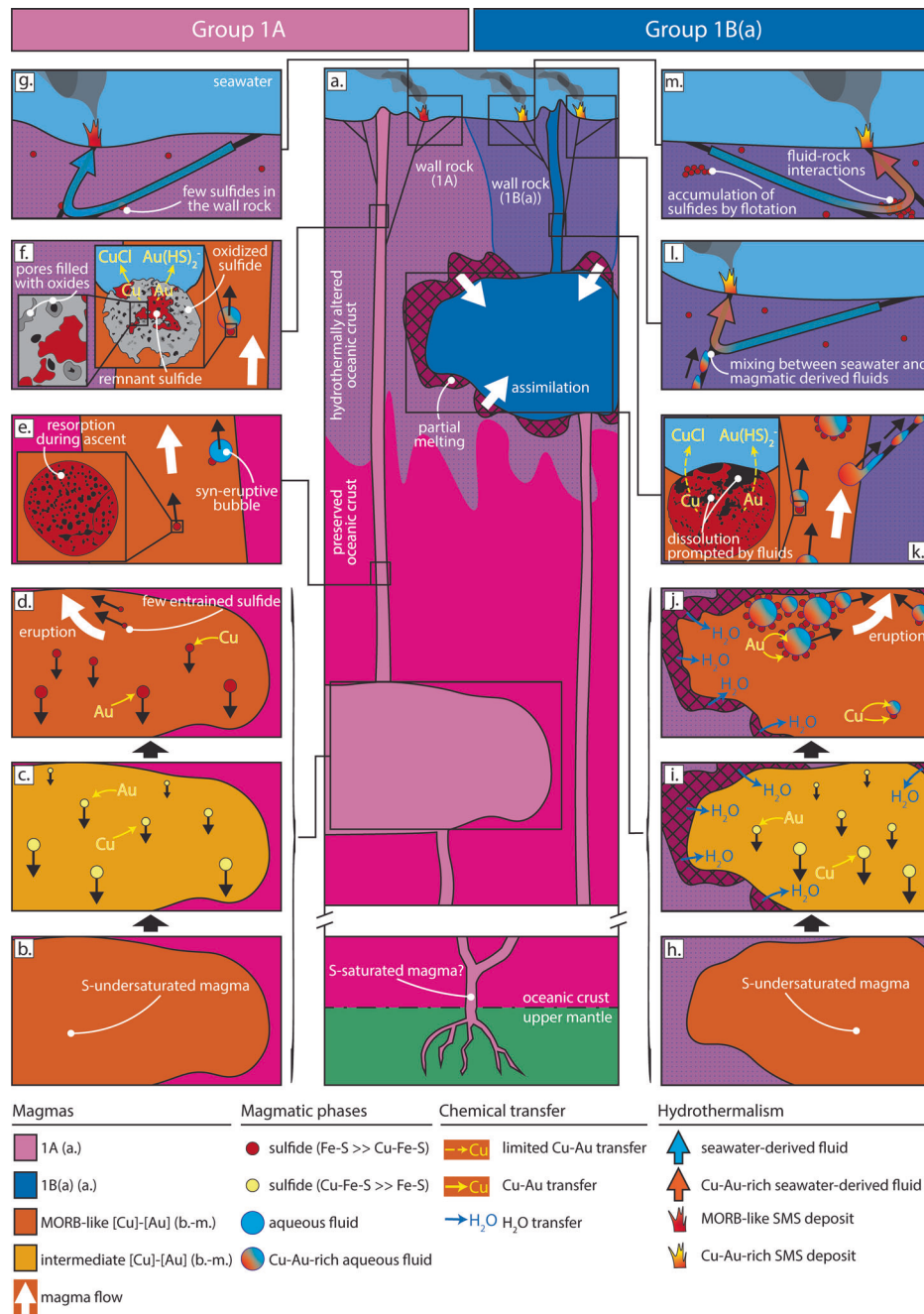


Fig. 6 | Cu-Au transfer from mantle to surface at Fatu Kapa. a Schematic representation of the magmatic plumbing of groups 1A and 1B(a) magmas (not drawn to scale). Magmas generated at mantle depths are S-saturated and become S-undersaturated when they accumulate in the upper crust. In group 1A magmas, Cu-Au concentrations increase until they reach sulfide saturation at intermediate stages (b, c). These elements are mainly trapped in the crust in Cu-rich sulfides (c), and thereafter in Fe-S sulfide blebs (d). However, some few small sulfides formed shortly before eruption may be entrained upward by erupting magmas (d, e, f). During ascent, sulfides partly dissolve (inset in e). Aqueous fluid bubbles may nucleate on sulfides during ascent, prompting sulfide oxidation (inset in f). In this process, Cu-Au are released from the sulfide into the bubble, but limited presence of sulfide-bubble droplets restricts considerable increase of Cu-Au content in the magmatic fluid. Because only a few sulfides rise to the surface, associated SMS deposits are not substantially enriched in Cu-Au (g). In group 1B(a) magmas, Cu-

Au concentrations initially increase until sulfide saturation is reached (h, i), with initial formation of Cu-Fe sulfides trapping Cu-Au in the crust (i). The addition of H₂O to the system through the assimilation of hydrothermally altered wall rock leads to volatile saturation at depth, occurring soon after sulfide saturation when Cu-rich sulfides (not shown) or more likely Fe-S sulfides (j) are formed. Cu-Au also partition into fluids as copper chloride (CuCl) and gold hydrosulfide (Au(HS)²⁻) complexes. Bubbles and sulfides nucleate on each other to form compound drops, which accumulate at the roof of the magmatic chamber and are entrained in erupting magmas. During their ascent, sulfide blebs are dissolved by aqueous fluids, but this process is limited due to the slight pressure drop encompassed by sulfide droplets during ascent (k). The Cu-Au endowment of Fatu Kapa SMS deposits is the result of both mixing between magmatic and seawater-derived hydrothermal fluids (l) and the leaching by hydrothermal fluids of preserved sulfides brought by flotation (m).

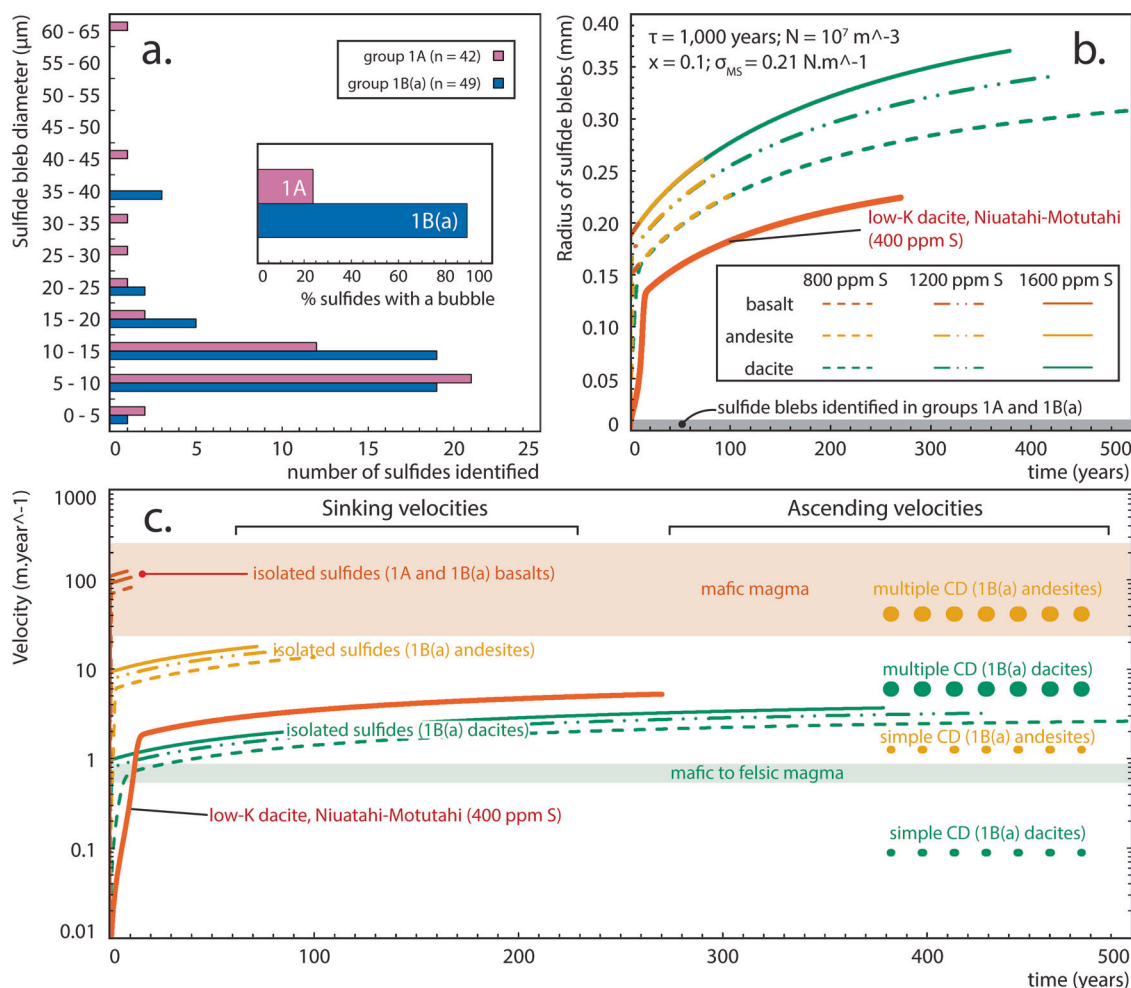


Fig. 7 | Size and sinking velocity of isolated magmatic sulfides within Fatu Kapa magmas compared to ascending velocities of compound drops and magmas.

a Histogram depicting the distribution of sulfide bleb diameters observed in the magmas of groups 1A and 1B(a). The proportions of sulfides associated with a bubble for groups 1A and 1B(a) are shown in the inset. **b** Mean sulfide droplet radius as a function of time for various initial sulfur concentrations estimated with a model of sulfide growth by diffusion and convection⁵⁵. Three initial S concentrations (800 ppm—dashed curves, 1200 ppm—dashed dotted curves, and 1600 ppm—solid curves) relevant to those found in natural systems are considered for basaltic (red curves), andesitic (orange curves) and dacitic (green curves) lavas akin to those found at Fatu Kapa. The same model for isolated sulfides within Niuatahi-Motutahi low-K dacites is shown by the thick red-orange curve for S concentrations of 400 ppm (see Implications). The model stops when the sulfide bleb reaches 1 km

depth. The range of sulfide sizes identified in groups 1A and 1B(a) are outlined by the gray rectangle. τ is the cooling timescale, N is the initial number density of sulfide nuclei, x is the degree of supersaturation required to form the sulfide nuclei, and σ_{MS} is the silicate melt-sulfide surface tension. Magma viscosities are estimated via ref. 68 (Table 1). **c** Velocity versus time for isolated sinking sulfides, ascending simple compound drops (lined smaller circles to the right), and ascending multiple compound drops (lined bigger circles to the right), compared to the ascending rates of mafic magmas within the crust⁵⁶ (redish rectangle) and to the velocities estimated from the mafic-silicic differentiation timescale⁵⁶, assuming a crustal section of 25 km (greenish rectangle). Sulfide sinking velocities are estimated with the same model as in **b**. CD compound droplets.

owing to an ascending rate for mafic magmas in the range of $\sim 20\text{--}300\text{ m year}^{-1}$ ⁵⁶. Conversely, most of the segregated sulfides formed between eruptions quickly attained a sinking velocity within the range of ascending magma velocities, supporting that they settled at the bottom of the magmatic chamber and scavenged Cu and Au from the magma body (Fig. 6c, d). Due to pressure drop experienced by magmas en route to the surface⁵⁷, syn-eruptive fluid bubbles may have nucleated on these entrained sulfides in the magmatic conduit (Fig. 6e), explaining the rare observations (10 total, inset in Fig. 7a) of compound drops in group 1A magmas.

As the few entrained sulfides in group 1A magmas rise toward the surface, they partially dissolve due to decreasing pressure^{48,58}. This is evidenced by the uniformly porous texture displayed by the pyrrhotitic phases within isolated sulfides (Supplementary Fig. 4 and Fig. 6e). Moreover, the rare sulfides attached to a syn-eruptive bubble in group 1A magmas may also undergo oxidation during ascent prompted by aqueous fluids confined

within the bubble. In all likelihood, Cu and Au in the compound drop are transferred from the sulfide to the bubble fluids during oxidation (Figs. 2 and 6f). The filling of resorbed pores with secondary oxides strongly suggests that sulfide oxidation occurs after sulfide dissolution.

Two processes are often considered in explaining the Cu-Au endowment of SMS deposits. The first involves mixing seawater-derived hydrothermal fluids with aqueous magmatic fluids^{10,12,24,25}. The second process relies on fluid-rock interactions between seawater-derived hydrothermal fluids and magmatic sulfides captured in lava host rocks^{11,13,25}. For group 1A magmas, the oxidation of sulfides connected to syn-eruptive bubbles could potentially increase the Cu and Au contents in the magmatic fluids released during ascent. However, this is likely limited since only one quarter of the sulfide blebs in group 1A is associated with bubbles, and most show minimal to no oxidation. Additionally, most sulfides formed in the magmatic chamber remain trapped at depth, limiting the opportunity for hydrothermal fluids to mobilize Cu and Au (Fig. 6g). Therefore, it is unlikely that

group 1A magmas considerably contributed to the Cu-Au endowment of the Fatu Kapa SMS deposits.

Similarly to group 1A magmas, we speculate that group 1B(a) magmas evolved firstly under S-undersaturated conditions, allowing an initial increase of Cu and Au concentrations ($0.5 < Th < 1.5$ ppm; Fig. 6h, i). Sulfide saturation occurs at the andesitic stage, with the sulfide phase initially forming in the Cu-Fe-S system and subsequently in the Fe-S system. We modeled the evolution of the sinking velocity of sulfide blebs over time in both andesitic and dacitic 1B(a) magmas (see Methods). In dacites, isolated sulfides quickly reach a sinking velocity of ~ 2 m year⁻¹ (Fig. 7c). The timescale span in the crust by mafic magmas evolving toward felsic compositions typically falls within 30,000–50,000 years^{56,59}. Considering a crustal section of 25 km, the average ascending velocity for these magmas ranges from 0.50 to 0.83 m year⁻¹. This implies that isolated sulfides within the dacitic 1B(a) magmas sink faster than the magmas ascend. In andesites, isolated sulfides quickly reach a sinking velocity of ~ 10 m year⁻¹ (Fig. 7c), which is close to the minimum ascending velocity of ~ 20 m year⁻¹ for magmas traversing the crust with limited compositional evolution. Consequently, it is likely that the sinking velocities of isolated sulfides within these andesitic magmas outpace the ascending velocities estimated from basaltic to andesitic storage timescales within the crust. Therefore, Cu and Au that would partition into isolated sulfides formed within andesitic to dacitic 1B(a) compositions will not be transferred to the seawater-derived hydrothermal system.

One key difference between groups 1B(a) and 1A magmas is the assimilation of the felsic water-rich magma endmember in group 1B(a) magmas. This addition of large amounts of water in the shallow magmatic plumbing enables the synchronous formation of volatile-rich bubbles and sulfide (Fe-S) blebs before eruption. In our VS4 and VS3 models, some of the Cu-rich sulfides are segregated before volatile saturation and are likely to be scavenged in the crust (Fig. 5a, b, c, Fig. 6i). After this stage, aqueous fluid bubbles and sulfide melts systematically stick together to form compound drops (inset in Fig. 7a). Multiple compound drops (e.g., Fig. 2d) ascend with a velocity of ~ 50 and ~ 5 m year⁻¹ within andesitic and dacitic 1B(a) magmas, respectively (Fig. 7c, see Methods). Because near vitreous 1B(a) samples contain only a few silicate minerals (Table 1, Supplementary Fig. 11), we suggest that capillary forces acting against multiple compound drop upwelling are limited, allowing their effective flotation. Once accumulated at the top of the magma chamber, these sulfides can be readily carried up by batches of erupting magmas (Fig. 6j). Simple compound drops (e.g., Fig. 2b) exhibit ascending velocities more than one order of magnitude lower than those estimated for multiple compound drops (~ 1.0 and ~ 0.2 m year⁻¹ in andesitic and dacitic magmas, respectively). While these simple compound drops are either neutrally buoyant or ascend slowly compared to magma ascent rates, they still facilitate the transport of sulfides towards the surface by preventing sulfide settlement.

Volatile saturation in these samples occurs when Cu, Pd, and presumably Au concentrations are still higher than those measured in MORB. Group 1B(a) magmas, which have elevated Cl concentrations, can partition Cu into aqueous fluids as copper chloride (CuCl) complexes^{60,61}. These magmas are relatively reduced ($\Delta FMQ < 0.4$), which may also promote the partitioning of Au into fluids as gold hydrosulfide (Au(HS)₂) complexes⁶². Therefore, in group 1B(a) magmas, a substantial portion of Cu and Au is transferred directly into aqueous fluids alongside partitioning in floating sulfides (Fig. 6j). We have demonstrated that during magma ascent, sulfide dissolution is prompted by aqueous fluids, as evidenced by pronounced porosity near bubbles (Figs. 2b and 6j). However, this process alone is unlikely to considerably increase Cu and Au concentrations in aqueous fluid bubbles. The preservation of over $\sim 80\%$ of initial sulfide volume suggests limited dissolution, likely due to the slight pressure drop during ascent from shallow 1B(a) magma chambers ($\sim 1.9 \pm 2.2$ km). Additionally, identification of Cu-rich phases at the sulfide/bubble interface (Fig. 2b) indicates that S, rather than Cu or Au, is transferred to the bubble during sulfide destabilization. Finally, the limited pressure drop, which implies that less aqueous fluids interact with sulfides^{19,26,28,30}, likely accounts for the scarcity of oxidized

sulfides, even though the majority of sulfides are linked to bubbles in this group.

Ultimately, the mixing of Cu-Au-rich magmatic fluids formed from group 1B(a) magmas with hydrothermal fluids (Fig. 6l) and the leaching of preserved 1B(a) sulfide blebs brought toward the surface through flotation (Fig. 6m) participate to the Cu-Au endowment of the Fatu Kapa SMS deposits.

Implications for the genesis of Cu-Au-rich SMS deposits in intra-oceanic subduction settings

Our study supports the idea that sulfide-bubble compound drops form when a magma is both volatile and S-saturated^{26,27}. In the Fatu Kapa magmas, sulfide flotation is essential to explain the Cu-Au endowment of the associated SMS deposits. This finding provides insights into the formation of Cu-Au-rich SMS deposits in ocean-ocean subduction settings. The rear-arc volcano Niuatahi-Motutahi, associated with Cu-Au-rich hydrothermal deposits⁶³, exemplifies the role of sulfide flotation in the Cu-Au endowment of SMS deposits in intra-oceanic subduction settings. Initially oxidized mafic magmas ($\Delta FMQ + 1.0 \pm 0.3$) prevent early S-saturation. Therefore, as magmatic differentiation operates, Cu and Au concentrations rise until magnetite crystallization initiates at the dacitic stage. The highest Cu contents in this magmatic suite are ~ 250 – 300 ppm, which is about twice as high as in group 1B(a) and about four times higher than in MORB (Fig. 1a)¹². Magnetite crystallization reduces ferric to ferrous iron, making the melt more reduced, favoring S²⁻ over S⁶⁺ stabilization, and triggering sulfide saturation¹². With such a high Cu content at the onset of sulfide saturation, the segregated sulfide phase is Cu-rich^{4,50,51}, consistent with the observation of Cu-rich sulfide blebs in Niuatahi-Motutahi dacites¹². The formation of aqueous fluids (MgO ~ 2 wt%) occurs shortly after the onset of sulfide saturation (MgO ~ 2.5 wt%). Given the elevated Cu and Au contents of these melts, their high chlorinity, and their decreasing fO_2 upon magnetite saturation, magmatic fluids formed at depth are likely Cu-Au-rich, with Cu forming CuCl complexes and Au forming hydrosulfide complexes. Additionally, since magmas at the onset of volatile saturation still exhibit Cu concentrations exceeding 100 ppm, it is probable that the sulfide phase remains Cu-rich. Since Cu-rich segregation and volatile saturation occur simultaneously, similar to 1B(a) magmas, aqueous fluid bubbles and sulfides may stick together within the dacitic magmatic chamber. We conducted modeling on the sinking velocity of isolated sulfides to examine whether they are entrained by the felsic upwelling magmas (see Methods). Our model shows that isolated sulfides quickly sink faster than magmas ascend, precluding the efficient transport of isolated sulfides by upwelling magmas. The efficient extraction of Cu and Au occurs through the segregation of sulfide liquids coupled with sulfide flotation, transporting these elements from magmas to the surface. Most ascending sulfides undergo complete oxidation or dissolution, transferring Cu and Au from sulfides to bubbles due to a considerable pressure drop between the magmatic chamber and the ocean floor (i.e., a larger amount of magmatic fluids interacting with sulfides) compared to that experienced by group 1B(a) sulfides (Fig. 4b). This explains the scarcity of magmatic sulfides in subsurface lavas sampled at Niuatahi-Motutahi¹². Identification of late sulfide saturation in other submarine slab-coupled back-arc and arc magmas associated with Cu-Au-rich ores, such as those in Pual Ridge^{10,11,24} and Valu Fa Ridge¹³ (Fig. 1a), suggests that this ore-forming mechanism is likely widespread, regardless of whether sulfide saturation is triggered by magnetite crystallization^{11–13} or by other factors^{14,50,64,65}.

Conclusions

By directly applying the Stoke's law to sulfides with diameters of 10 and 100 μ m, it has been suggested that most sulfide blebs, particularly within intermediate and felsic systems, are entrained by upwelling magmas without requiring bubble attachment and subsequent flotation²⁹. Nevertheless, our investigation, which incorporates realistic models of sulfide growth and plausible timescales of magmatic evolution within the crust, challenges this assumption, particularly in intra-oceanic settings. We find that segregated

sulfides tend to sink regardless of whether the magmas are mafic or felsic, which involves that the timing between sulfide droplets and aqueous fluid bubbles formation emerges as the primary parameter governing Cu-Au transfers from magmas to the surface. In scenarios where S-saturation occurs substantially earlier than volatile saturation (e.g., group 1A), Cu-Au partition into sinking sulfides only and are not effectively transferred to the surface. In cases where S-saturation precedes volatile saturation by a shorter interval (e.g., group 1B(a)), only a small portion of Cu-Au is lost through partitioning within Cu-rich sulfides, while a considerable amount is transferred to the surface by partitioning into both aqueous fluids and floating Fe-S sulfides. Lastly, in instances where S-saturation occurs within Cu-rich volatile-saturated magmas (e.g., Niuatahi-Motutahi), most of the Cu-Au content within the magmatic chamber is efficiently transferred toward the surface via partitioning into both aqueous fluids and floating Cu-rich sulfides.

Methods

Models of Cu, Pd, Zn, Pb, and Co concentrations

Initial compositions, stages of magmatic evolution, and the partition coefficients employed are summarized in Supplementary Tables 2–5 and Supplementary Note 4.

Group 1A

Reverse modeling of major elements and forward modeling of lithophile trace elements have revealed that group 1A magmas primarily evolve by fractional crystallization of an olivine-plagioclase-clinopyroxene-rich cumulate throughout their evolution³⁹. In lavas characterized by Th values that are less than 2 ppm (cumulate A), oxides are present in minimal amounts. Conversely, for lavas with Th values exceeding 2 ppm, ~12% of the cumulate composition consists of oxides (cumulate B). To address the behavior of chalcophile elements, we divided the evolution of group 1A magmas into four distinct stages, each of which is described below. During each stage, we modeled the behavior of these elements using the fractional crystallization Eq. (1), where F represents the residual melt fraction, C_L denotes the concentration of an element in the residual melt, C_L^0 stands for the concentration of the element in the parental melt, and D represents the bulk partition coefficient for that element.

$$\frac{C_L}{C_L^0} = F^{D-1} \quad (1)$$

Stage 1. From 0.50 to 0.70 ppm Th, 1A magmas are S-undersaturated and we employed the same mode as cumulate A.

Stage 2. Starting from 0.70 ppm Th ($F = 0.7$), the Pd content of group 1A magmas substantially decreases as Th values increase, indicating that S-saturation has been reached. Recent experimental findings have shown that when the Cu content in the silicate magma is higher than ~100 ppm, the segregated sulfide phase is mainly a Cu-Fe-S phase, whereas mixtures of Fe-S and Cu-Fe-S phases are segregated below this value⁴. This conclusion is further supported by the observation that more than 50% of Cu-rich sulfides are needed to account for the crystallization paths of Cu and Pd in magmatic suites showing Cu contents exceeding ~100 ppm⁴. In contrast, a proportion of less than 20% Cu-rich sulfides is required for magmas with lower Cu content^{4,39,50,51}. This aligns with the identification of predominantly Cu-rich sulfides in the Cu-rich silicate melt at the onset of sulfide saturation and the identification of Cu-poor sulfides as these magmas become Cu-depleted⁵⁰. Given that group 1A magmas reach up to ~160 ppm Cu during their S-undersaturated stage of evolution, we slightly changed the mode of cumulate A to take into account the segregation of 0.19% sulfides with a Cu-Fe-S:Fe-S proportion of 85:15 until the Cu value reaches ~120 ppm Cu (~0.83 ppm Th).

Stage 3. From ~0.83 ppm Th to 2 ppm Th, Pd, and to a lesser extent Cu, exhibit decreased compatibility with further magmatic evolution. This suggests that the proportion of the Cu-Fe-S phase compared to the Fe-S phase is lower in the segregated phase. Additionally, the Cu-Fe-S:Fe-S proportion in the magmatic sulfides identified in lavas with 1.5 ppm and 2.0 ppm Th varies in the range of 0:100 to 20:80. Therefore, for stage 3, we maintained the same cumulate mode as in stage 2 but adjusted the Cu-Fe-S:Fe-S proportion from 85:15 to 5:95.

Stage 4. Starting from 2 ppm Th, the composition of the cumulate shifts from cumulate A to cumulate B³⁹. Consequently, we made slight adjustments to the mode of cumulate B to incorporate the same amount of segregated sulfides as in stages 2 and 3, with the same Cu-Fe-S:Fe-S proportions as in stage 3. This four-stage model of fractional crystallization effectively reproduces the measured concentrations of Cu, Pd, Zn, and Pb (Fig. 5).

Group 1B(a)

Direct modeling on lithophile trace elements (e.g., REE, Zr, Ba, U) of group 1B(a) has shown that pure mixing between a basaltic magma from group 1A and a Th-rich felsic endmember generated by 25% partial melting of an intermediate magma from group 1A satisfactorily explains the evolution of these incompatible elements³⁹. However, the presence of plagioclases, clinopyroxenes, and oxides (Supplementary Fig. 11) as well as that of magmatic sulfides (Fig. 2) in the glassy samples of group 1B(a) suggests that fractional crystallization must be considered when modeling the evolution of elements that are compatible with these phases. For this reason, the Eq. (2) of assimilation coupled with fractional crystallization (AFC)⁵² may appear suitable for modeling the evolution of compatible elements. In this equation, C_L , C_L^0 and F have the same meaning as in Eq. (1), r represents the ratio between the assimilation rate and the fractional crystallization rate, z is defined as Eq. (3), where D is the same as in the Eq. (1), and C_a stands for the concentration of the element in the wall rock. However, no AFC model tested can adequately account for the high Th content of group 1B(a) magmas because these models implicitly assume a melting degree of 100% (i.e., the composition of the assimilated magma equals that of the wall rock)³⁹. This implies that the assimilated magmas could not exhibit higher Th values than the wall rock. To address this limitation and to model the mixing of the fractionating magma with a Th-rich magma generated by partial melting with a degree different than 100%, Eq. (2) was combined with the batch partial melting Eq. (4) to create a fractional crystallization model coupled with assimilation of a magma generated by partial melting (FC-PMA). In Eq. (4), C_w stands for the concentration of the element in the melted wall rock, D_w is the bulk partition coefficient of the wall rock and F_{PM} represents the rate of partial melting. Consequently, the evolution of Th, Zn, and Pb was modeled using the FC-PMA model. However, for highly chalcophile elements, their behavior during partial melting can be variable depending on the presence and nature of residual sulfides. Nevertheless, given that the initial Cu and Pd contents in altered crust are low and the dilution effect due to assimilation is negligible at the low r value of 0.15 that we selected (see below), we decided to apply the AFC model (i.e., $C_a = C_w$) to account for the evolution of Cu and Pd.

$$\frac{C_L}{C_L^0} = F^{-z} + \frac{r}{r-1} \frac{C_a}{zC_L^0} (1 - F^{-z}) \quad (2)$$

$$z = \frac{r + D - 1}{r - 1} \quad (3)$$

$$C_a = \frac{C_w}{D_w + F_{PM}(1 - D_w)} \quad (4)$$

To model the evolution of compatible lithophile elements, we utilized the same wall rock composition, bulk partition coefficients of the wall rock, and rate of partial melting as required for modeling the evolution of incompatible lithophile elements (i.e., the melted sample is the intermediate rock FU3-DR-13-05 from group 1A, $D_w = \text{cumulate B}$, and $F_{PM} = 25\%$)³⁹. To determine the value of r , we applied the following model to non-chalcophile to moderately chalcophile elements, specifically La, Sm, Eu, Dy, and Co, for various r values (Supplementary Fig. 10). The evolution of the REE is well-reproduced for r values above 0.1. However, due to their incompatible behavior, REE concentrations become primarily controlled by the composition of the assimilated magma, making it challenging to distinguish between higher r values. The trend of Co, which exhibits strong compatibility with oxides, matches well with a r value of 0.15. As a result, we selected an r value of 0.15 to model the evolution of Cu, Pd, Zn, Pb, and Th. We employed the same initial melt composition as used for group 1A.

Similar criteria to those applied for group 1A were used to model the behavior of metals in group 1B(a) magmas through volatile undersaturated conditions (blue line in Fig. 5). Once sulfide saturation occurs, the sulfide phase is primarily composed of sulfide liquid for Cu values above ~120 ppm (with a Cu-Fe-S:Fe-S proportion of 90:10) and shifts to a predominance of Fe-S below this threshold (with a Cu-Fe-S:Fe-S proportion of 15:85), with 0.22 wt% of sulfides formed. This latter Cu-Fe-S:Fe-S balance is consistent with the proportions observed in group 1B(a) sulfides (Fig. 2, Supplementary Figs. 4, 5). We adopted silicate and oxide proportions similar to those of cumulate A for Th concentrations below 2 ppm and similar to those of cumulate B for higher Th concentrations. Since the initial melt composition is the same as for group 1A, sulfide saturation is initiated when the F value reached $0.7 \pm 10\%$. This uncertainty of 10% accounts for potential variations in melt volumes due to assimilation and differences in pre-eruptive pressures between group 1B(a) magmas and those of group 1A. This uncertainty is depicted by the sheaths of the Cu and Pd trends (Fig. 5a, b) and does not considerably affect the behavior of Th, Pb, and Zn (Fig. 5).

To model the evolution of group 1B(a) magmas under volatile-saturated conditions with the VS5, VS4, VS3, and VS2 scenarios, we estimated the Th value at the onset of volatile saturation, defined as the Th value for which the modeled water concentration reaches water saturation (i.e., $\text{H}_2\text{O} = 2.1 \text{ wt}\%$, (Fig. 4)). These Th values are equal to 1.40, 1.55, 1.85, and 2.20 ppm in the scenarios VS5, VS4, VS3, and VS2, respectively. The amount of fluid formed in each scenario is calculated as the difference between the modeled and estimated water content in group 1B(a) magmas at a Th value of ~3.7 ppm. We applied the same criteria for the evolution of chalcophile elements as used in the volatile-undersaturated case, with slight modifications to the proportions of silicate minerals to account for formed fluids. It is worth noting that when volatile saturation occurs before sulfur saturation or during the stage of sulfide segregation, as is the case for scenarios VS4 to VS3, the partitioning of Cu into aqueous fluids shortens the stage of Cu-Fe sulfide segregation. This explains why the calculated trends for Pd vary from one scenario to another, even though this element does not considerably partition into aqueous fluids^{16,66}.

Models of sulfide growth and sinking velocities

We adapted a pre-existing model⁵⁵ of sulfide growth and related sinking velocity to isolated sulfides in the basaltic magmas of group 1A. Parameters similar to those utilized in another study²⁷ were adopted, including the diffusivity of sulfur in mafic melt following the experiments of Freda et al.⁶⁷, a surface tension between silicate liquid and sulfide (σ_{MS}) of 0.21 N m^{-1} , an initial number density of sulfide nuclei of 10^7 m^{-3} , a supersaturation degree (x) of 0.1, and a cooling timescale (τ) of 1000 years. The viscosity of a basalt from group 1A was estimated using a viscosity calculator⁶⁸ (Table 1). The Hadamard–Rybczynski version of the Stokes equation was used to estimate sulfide velocities. We considered three initial S concentrations (800 ppm, 1200 ppm, and 1600 ppm) relevant to those observed in natural systems, and the model was terminated when a settling depth of 1 km was attained, corresponding to a standard magmatic chamber depth^{55,69}.

We modeled the evolution of the sinking velocity of sulfide blebs over time in both andesitic and dacitic 1B(a) magmas using a similar model to the one employed for group 1A sulfides, adapting the magma viscosities to those estimated for these lavas (Table 1). As we did not directly sample the andesitic lavas in group 1B(a), we utilized the major element concentrations of an andesite from group 1A and relied on the assumption that these magmas are near volatile saturation (i.e., H_2O concentration equal to water solubility) to estimate their viscosity.

We adapted this model to sulfides present in the volatile saturated low-K dacites erupted at Niutahi-Motutahi (Tonga rear-arc)¹². These low-K dacitic magmas are stored at an average pressure of $1.9 \pm 0.7 \text{ kbar}$ ($n = 11$)¹², corresponding to a minimum water solubility of ~4.3 wt% (Fig. 4b). We utilized this minimum water solubility to estimate the maximum viscosity of these lavas, which amounts to ~850 Pa·s at a temperature of 1000 °C. This temperature falls within the range of 960–1040 °C estimated for these lavas¹². We used a S concentration equal to 400 ppm, in agreement with measurements within melt inclusions¹².

Estimation of compound drop densities and velocities

Two abaci were established to determine the density of sulfide-bubble compound drops based on their θ_{MV} angle²⁷. The θ_{MV} angle represents the angle between the line connecting the center of the sulfide to the center of the bubble and the line connecting the center of the bubble to the sulfide-bubble-silicate melt interface. The first abacus corresponds to the cases where the surface tension between silicate melts and vapor bubbles equals 0.18 N m^{-1} , while the second abacus corresponds to the cases where this surface tension is equal to 0.36 N m^{-1} . These values encompass the minimum and maximum surface tension estimated in natural systems. The θ_{MV} angle of compound drops was measured from SEM images and plotted in these two abaci to estimate the minimum and maximum density of compound drops. In the case of ellipsoidal-shaped bubbles, the θ_{MV} angle was determined as the average value between $\theta_{MV \text{ min}}$ and $\theta_{MV \text{ max}}$, where $\theta_{MV \text{ min}}$ and $\theta_{MV \text{ max}}$ represent the θ_{MV} angles corresponding to the circle with the smallest and largest radii of the ellipsoid, respectively.

For bubbles associated with a single sulfide, the density of the compound drop falls within the range of 351 and 492 kg m^{-3} (16 densities estimated), and we selected a value of 400 kg m^{-3} . We estimated the ascending velocities of these compound drops with the Hadamard–Rybczynski version of the Stokes equation (Table 1). In our calculations, we simplified the shape of compound drops by assuming a spherical form with a volume representative to that of the observed bubble, namely $45 \mu\text{m}$ (Fig. 2b).

For estimating the ascending velocity of multiple compound drops, we used the same density as for simple compound drops, although this value is likely lower given the wider size of the bubbles. We used a bubble diameter of $260 \mu\text{m}$ (Fig. 2d).

Analytical methods

The Cu concentration in the magmatic glasses. Cu concentrations in 20 magmatic glasses were determined by laser ablation inductively coupled mass spectrometry (LA-ICPMS) at the *Institut Universitaire Européen de la Mer (Pôle Spectrométrie Océan, Brest, France)*. The samples consisted of polished sections of silicate glass chips, except for the glassy sample FU2-DR27-03, which had its composition determined from measurements on a polished thin section. The analytical setup included a COMPexPro excimer laser ($\lambda = 193 \text{ nm}$) coupled with an Element XR ICP-MS system. For each sample, three to eight measurements of the mass ⁶⁵Cu were performed and quantified using the NIST SRM 612 glass as a reference material⁷⁰. ⁴³Ca served as an internal standard. The operating conditions were as follows: an ablation rate of 7 Hz in low-resolution mode ($m/\Delta m = 300$), a spot size of $90 \mu\text{m}$, 30 s of background measurement, and 100 s of ablation time. Reference materials such as the natural basaltic glasses BIR1g and BCR2g⁷¹ and the synthetic glass NIST SRM 614⁷² were used to ensure the accuracy of the measurements. The measured concentrations of these reference

materials were found to be within their 2σ certified standard deviation (Supplementary Table 6). The reproducibility (%RSD) for Cu was 4%, 8%, and 49% with the BIR1g, BCR2g and NIST SRM 614 materials, respectively.

The Cu and Zn concentrations in the magmatic whole rocks. Cu and Zn concentrations in 28 magmatic whole rock samples, as well as Cu, Zn, Pb, and Au concentrations, were determined by wavelength-dispersive X-ray fluorescence spectrometry (WD-XRF) at the Laboratory Bio-Geochemical cycles and Resources laboratory (Ifremer, Brest, France). The analysis was performed with a Bruker AXS S8 TIGER system for fusion beads. After data acquisition, the measured net peak intensities were corrected for inter-element effects and converted into concentrations. The conversion was achieved using calibration curves generated from the analysis of geochemical standard powders, which were measured under identical analytical conditions. Additionally, further analyses of Cu and Zn in the magmatic whole rock samples were carried out using inductively coupled plasma mass spectrometry (ICP-MS) at Geo-Labs (Ontario, Canada).

The Pd concentration in the magmatic whole rocks and glasses. Pd concentrations in 11 replicated whole rocks and 7 replicated powdered glasses were measured by a quadrupole ICP-MS after sample preparation of the Ni-sulfide fire assay-isotope dilution (NIS-FA-ID) method⁷³. A 5 g split of the powder was mixed with Ni, S, and sodium borax with a ratio of sample:Ni:S:borax of 10:1:0.5:10. An enriched PGE spike solution (¹⁰⁵Pd) was added to the mixture. The spiked powder mixtures were dried at 100 °C for 1 h and fused for 20 min in an open furnace preheated to 1150 °C. N₂ gas was introduced into the furnace, and a second outer crucible containing ~0.8 g of flour was used for reducing conditions during fusion. The fused melts were then quenched by removing the crucible from the furnace. Sulfide beads were recovered from the quenched glasses and dissolved in 6 M HCl. The solution was passed through a filter paper (0.45 μm cellulose membrane), on which PGE-bearing particles were collected. The filter paper was digested in 4 mL of aqua regia, and the final solution was dried down to <0.1 mL and diluted with 2% HCl.

An Agilent 8900 Triple Quadrupole ICP-MS at Seoul National University (Seoul, South Korea) was used to analyze Pd concentrations. The molecular interferences on the analyte elements by metal oxides, argides, and chloride were monitored by analyzing single element solutions containing Cu, Mo, Zn, and Zr. The oxide, argide and chloride production rates were 0.05–0.5%, 0.001–0.003%, and 0.0004%, respectively. The interference correction for Pd is <0.5% for 16 samples, from 0.5 to 2% for 15 samples, and from 2 to 7% for 5 samples. Concentrations were determined by the isotope dilution method using the ¹⁰⁵Pd/¹⁰⁸Pd ratio.

Procedural blanks were measured from the sample-free analyses ($n = 18$). The average procedural blanks are 182 ± 70 pg Pd. The Pd method detection limit (MDL) was taken to be one standard deviation of the procedural blanks. Pd MDL for samples is 14 ppt for 5 g samples. The procedural blank values used to calculate averages and the detailed MDL information are shown in Supplementary Table 7. The accuracy and precision of the analyses were checked by six measurements of a reference material TDB-1⁷⁴ and the results are listed in Supplementary Table 8. The measured TDB-1 values are consistent with literature values within 1σ for all. The %RSD is 3% for Pd.

The FeO/FeO_{total} ratio in the magmatic glasses. The FeO concentration in 14 magmatic glasses was determined using the direct titration method⁷⁵. Approximately 0.5 mg of glass powders were dissolved in a boiling mixture of sulfuric and hydrofluoric acids for 3 min. The ferrous iron released during dissolution was immediately titrated against a potassium dichromate solution in a mixture of H₂SO₄ and H₃PO₄, with barium diphenylamine sulfonate used as the redox indicator.

The FeO_{total} content of these solutions was determined after boiling using inductively coupled plasma atomic emission spectroscopy (ICP-AES) at the *Laboratoire de Planétologie et Géosciences* (Nantes, France). After data acquisition, the measured intensities were converted into concentrations using calibration curves generated from the analysis of geochemical standard solutions, which were measured under identical analytical conditions. The FeO_{total} content of the certified W-2 standard was measured six times, yielding a value of 9.72 ± 0.03 wt% (1σ), which falls within the GEOREM certified value of 9.72 ± 0.04 wt%.

Major element concentrations in the sulfide droplets. Major element concentrations of 90 sulfide droplets, including Si, S, Fe, Zn, Cu, Ni, and Co, were determined using an electron microprobe (CAMECA SX100, *Microsonde Ouest*, Brest, France) on carbon-coated polished thin sections with a thickness of 100 μm. The analytical conditions were as follows: 15 kV accelerating voltage, 10 nA beam current, 1 μm spot size, and 10 s counting time for Si, S, Fe, Zn, 20 s for Cu and Ni, and 30 s for Co. Silicon was also measured to confirm the absence of silicate phases surrounding the sulfide blebs within the analyzed volume.

Additional data used in this study. The concentrations of Co, Th, and Pb in magmatic glasses and whole rocks, as well as the major element concentrations in magmatic glasses, whole rocks, plagioclases, and clinopyroxenes, are those published elsewhere³⁹.

Collection of geological materials

Geological samples were collected by dredges and human operated vehicle Nautil operations in a responsible manner and in accordance with relevant permits and local laws.

Data availability

The dataset (glass and whole rock concentrations in chalcophile elements, textural description of magmatic sulfides and their concentration in major elements, thermobarometry results, thermohygrography results, average composition of SMS ores, and measured reference materials), as well as models generated for this study (geochemical models for the evolution of chalcophile element concentrations, models of sulfide growth and associated viscosity calculators) can be found on Figshare at the following <https://doi.org/10.6084/m9.figshare.26131333.v1>.

Received: 9 November 2023; Accepted: 16 July 2024;

Published online: 27 August 2024

References

- Hannington, M. D. De Ronde, C. E. & Petersen, S. Sea-floor tectonics and submarine hydrothermal systems. *Economic Geology* **100**, 111–141 (2005).
- Mungall, J. E. & Brenan, J. M. Partitioning of platinum-group elements and Au between sulfide liquid and basalt and the origins of mantle-crust fractionation of the chalcophile elements. *Geochim. Cosmochim. Acta* **125**, 265–289 (2014).
- Liu, Y. & Brenan, J. Partitioning of platinum-group elements (PGE) and chalcogens (Se, Te, As, Sb, Bi) between monosulfide-solid solution (MSS), intermediate solid solution (ISS) and sulfide liquid at controlled fO₂-fS₂ conditions. *Geochim. Cosmochim. Acta* **159**, 139–161 (2015).
- Li, Y., Audétat, A., Liu, Z. & Wang, F. Chalcophile element partitioning between Cu-rich sulfide phases and silicate melt and implications for the formation of Earth's continental crust. *Geochim. Cosmochim. Acta* **302**, 61–82 (2021).
- Candela, P. A. & Holland, H. D. The partitioning of copper and molybdenum between silicate melts and aqueous fluids. *Geochim. Cosmochim. Acta* **48**, 373–380 (1984).
- Keppler, H. & Wyllie, P. J. Partitioning of Cu, Sn, Mo, W, U, and Th between melt and aqueous fluid in the systems haplogranite-H₂O

- HCl and haplogranite–H₂O–HF. *Contrib. Mineral. Petrol.* **109**, 139–150 (1991).
7. Zajac, Z., Halter, W. E., Pettke, T. & Guillong, M. Determination of fluid/melt partition coefficients by LA-ICPMS analysis of co-existing fluid and silicate melt inclusions: Controls on element partitioning. *Geochim. Cosmochim. Acta* **72**, 2169–2197 (2008).
 8. Guo, H. & Audétat, A. Transfer of volatiles and metals from mafic to felsic magmas in composite magma chambers: an experimental study. *Geochim. Cosmochim. Acta* **198**, 360–378 (2017).
 9. Jugo, P. J. Sulfur content at sulfide saturation in oxidized magmas. *Geology* **37**, 415–418 (2009).
 10. Sun, W., Arculus, R. J., Kamenetsky, V. S. & Binns, R. A. Release of gold-bearing fluids in convergent margin magmas prompted by magnetite crystallization. *Nature* **431**, 975–978 (2004).
 11. Jenner, F. E., O'Neill, H. S. C., Arculus, R. J. & Mavrogenes, J. A. The magnetite crisis in the evolution of arc-related magmas and the initial concentration of Au, Ag and Cu. *J. Petrol.* **51**, 2445–2464 (2010).
 12. Park, J. W., Campbell, I. H., Kim, J. & Moon, J. W. The role of late sulfide saturation in the formation of a Cu- and Au-rich magma: insights from the platinum group element geochemistry of Niuatahi–Motutahi lavas, Tonga rear arc. *J. Petrol.* **56**, 59–81 (2015).
 13. Jenner, F. E. et al. The competing effects of sulfide saturation versus degassing on the behavior of the chalcophile elements during the differentiation of hydrous melts. *Geochem. Geophys. Geosyst.* **16**, 1490–1507 (2015).
 14. Scaillet, B., & Pichavant, M. A model of sulphur solubility for hydrous mafic melts: application to the determination of magmatic fluid compositions of Italian volcanoes. *Ann. Geophys.* **48**, 671–698 (2005).
 15. Li, C. & Ripley, E. M. Sulfur contents at sulfide-liquid or anhydrite saturation in silicate melts: empirical equations and example applications. *Econ. Geol.* **104**, 405–412 (2009).
 16. Wood, S. A. Thermodynamic calculations of the volatility of the platinum group elements (PGE): the PGE content of fluids at magmatic temperatures. *Geochim. Cosmochim. Acta* **51**, 3041–3050 (1987).
 17. Park, J. W., Campbell, I. H. & Kim, J. Abundances of platinum group elements in native sulfur condensates from the Niuatahi–Motutahi submagmatic volcano, Tonga rear arc: Implications for PGE mineralization in porphyry deposits. *Geochim. Cosmochim. Acta* **174**, 236–246 (2016).
 18. Park, J. W., Campbell, I. H. & Arculus, R. J. Platinum-alloy and sulfur saturation in an arc-related basalt to rhyolite suite: evidence from the Pual Ridge lavas, the Eastern Manus Basin. *Geochim. Cosmochim. Acta* **101**, 76–95 (2013).
 19. Nadeau, O., Williams-Jones, A. E. & Stix, J. Sulphide magma as a source of metals in arc-related magmatic hydrothermal ore fluids. *Nat. Geosci.* **3**, 501–505 (2010).
 20. Berlo, K., van Hinsberg, V. J., Vigouroux, N., Gagnon, J. E. & Williams-Jones, A. E. Sulfide breakdown controls metal signature in volcanic gas at Kawah Ijen volcano, Indonesia. *Chem. Geol.* **371**, 115–127 (2014).
 21. Edmonds, M., Mather, T. A. & Liu, E. J. A distinct metal fingerprint in arc volcanic emissions. *Nat. Geosci.* **11**, 790–794 (2018).
 22. Herzig, P. M., Hannington, M. D. & Arribas, A. Jr Sulfur isotopic composition of hydrothermal precipitates from the Lau back-arc: implications for magmatic contributions to seafloor hydrothermal systems. *Mineralium Depos.* **33**, 226–237 (1998).
 23. Seewald, J. S. et al. Submarine venting of magmatic volatiles in the eastern Manus Basin, Papua New Guinea. *Geochim. Cosmochim. Acta* **163**, 178–199 (2015).
 24. Kamenetsky, V. S. et al. Parental basaltic melts and fluids in eastern Manus backarc basin: Implications for hydrothermal mineralisation. *Earth Planet. Sci. Lett.* **184**, 685–702 (2001).
 25. Keith, M. et al. Constraints on the source of Cu in a submarine magmatic-hydrothermal system, Brothers volcano, Kermadec island arc. *Contrib. Mineral. Petrol.* **173**, 1–16 (2018).
 26. Mungall, J. E., Brenan, J. M., Godel, B., Barnes, S. J. & Gaillard, F. Transport of metals and sulphur in magmas by flotation of sulphide melt on vapour bubbles. *Nat. Geosci.* **8**, 216–219 (2015).
 27. Yao, Z. & Mungall, J. E. Flotation mechanism of sulphide melt on vapour bubbles in partially molten magmatic systems. *Earth Planet. Sci. Lett.* **542**, 116298 (2020).
 28. Le Vaillant, M., Barnes, S. J., Mungall, J. E. & Mungall, E. L. Role of degassing of the Noril'sk nickel deposits in the Permian–Triassic mass extinction event. *Proc. Natl Acad. Sci. USA.* **114**, 2485–2490 (2017).
 29. Heinrich, C. A. & Connolly, J. A. Physical transport of magmatic sulfides promotes copper enrichment in hydrothermal ore fluids. *Geology* **50**, 1101–1105 (2022).
 30. Iacono-Marziano, G., Le Vaillant, M., Godel, B. M., Barnes, S. J. & Arbaret, L. The critical role of magma degassing in sulphide melt mobility and metal enrichment. *Nat. Commun.* **13**, 2359 (2022).
 31. Kim, J. et al. Sulfide minerals and chalcophile elements in The Pleiades Volcanic Field, Antarctica: implications for the distribution of chalcophile metals in continental intraplate alkaline magma systems. *Contrib. Mineral. Petrol.* **178**, 67 (2023).
 32. Keele, R. A. & Nickel, E. H. The geology of a primary millerite-bearing sulfide assemblage and supergene alteration at the Otter Shoot, Kambalda, Western Australia. *Econ. Geol.* **69**, 1102–1117 (1974).
 33. Prichard, H. M., Hutchinson, D. & Fisher, P. C. Petrology and crystallization history of multiphase sulfide droplets in a mafic dike from Uruguay: implications for the origin of Cu–Ni–PGE sulfide deposits. *Econ. Geol.* **99**, 365–376 (2004).
 34. Hill, R. E. T., Barnes, S. J., Dowling, S. E. & Thordarson, T. Komatiites and nickel sulphide orebodies of the Black Swan area, Yilgarn Craton, Western Australia. 1. Petrology and volcanology of host rocks. *Mineralium Depos.* **39**, 684–706 (2004).
 35. Barnes, S. J., Wells, M. A. & Verrall, M. R. Effects of magmatic processes, serpentinization, and talc-carbonate alteration on sulfide mineralogy and ore textures in the Black Swan disseminated nickel sulfide deposit, Yilgarn Craton. *Econ. Geol.* **104**, 539–562 (2009).
 36. Holwell, D. A., Abraham-James, T., Keays, R. R. & Boyce, A. J. The nature and genesis of marginal Cu–PGE–Au sulphide mineralisation in Paleogene Macrodykes of the Kangerlussuaq region, East Greenland. *Mineralium Depos.* **47**, 3–21 (2012).
 37. Barnes, S. J., Le Vaillant, M., Godel, B. & Leshner, C. M. Droplets and bubbles: solidification of sulphide-rich vapour-saturated orthocumulates in the Norilsk–Talnakh Ni–Cu–PGE ore-bearing intrusions. *J. Petrol.* **60**, 269–300 (2019).
 38. Blanks, D. E. et al. Fluxing of mantle carbon as a physical agent for metallogenic fertilization of the crust. *Nat. Commun.* **11**, 4342 (2020).
 39. Jeanvoine, A., Chazot, G., Labanieh, S., Pelleter, E. & Fouquet, Y. Origin and evolution of the Fatu Kapa magmatic system (North-Western Lau Back-Arc Basin): insight on the genesis of high-silica lavas. *J. Petrol.* **62**, egab039 (2021).
 40. Moore, J. G., & Calk, L. Sulfide spherules in vesicles of dredged pillow basalt. *Am. Mineral. J. Earth Planet. Mater.* **56**, 476–488 (1971).
 41. Yeats, R. S. & Mathez, E. A. Decorated vesicles in deep-sea basalt glass, eastern Pacific. *J. Geophys. Res.* **81**, 4277–4284 (1976).
 42. Waters, L. E. & Lange, R. A. An updated calibration of the plagioclase-liquid hygrometer-thermometer applicable to basalts through rhyolites. *Am. Mineral.* **100**, 2172–2184 (2015).
 43. Putirka, K. D. Thermometers and barometers for volcanic systems. *Rev. Mineral. Geochem.* **69**, 61–120 (2008).
 44. Newman, S. & Lowenstern, J. B. VolatileCalc: a silicate melt–H₂O–CO₂ solution model written in visual basic for excel. *Comput. Geosci.* **28**, 597–604 (2002).
 45. Hao, H., Park, J. W. & Campbell, I. H. Role of magma differentiation depth in controlling the Au grade of giant porphyry deposits. *Earth Planet. Sci. Lett.* **593**, 117640 (2022).

46. Hao, H., Campbell, I. H., Arculus, R. J. & Perfit, M. R. Using precious metal probes to quantify mid-ocean ridge magmatic processes. *Earth Planet. Sci. Lett.* **553**, 116603 (2021).
47. Kiseeva, E. S. & Wood, B. J. The effects of composition and temperature on chalcophile and lithophile element partitioning into magmatic sulphides. *Earth Planet. Sci. Lett.* **424**, 280–294 (2015).
48. O'Neill, H. S. C. The thermodynamic controls on sulfide saturation in silicate melts with application to ocean floor basalts. in *Magma Redox Geochemistry* 177–213 (Wiley, 2021).
49. Ripley, E. M., Brophy, J. G. & Li, C. Copper solubility in a basaltic melt and sulfide liquid/silicate melt partition coefficients of Cu and Fe. *Geochim. Cosmochim. Acta* **66**, 2791–2800 (2002).
50. Costa, S. et al. Tracking metal evolution in arc magmas: Insights from the active volcano of La Fossa, Italy. *Lithos* **380**, 105851 (2021).
51. Costa, S. et al. Platinum-group element geochemistry of the shoshonitic igneous suite of Vulcano (Aeolian Arc, Italy): implications for chalcophile element fertility of arc magmas. *Contrib. Mineral. Petrol.* **176**, 106 (2021).
52. DePaolo, D. J. Trace element and isotopic effects of combined wallrock assimilation and fractional crystallization. *Earth Planet. Sci. Lett.* **53**, 189–202 (1981).
53. Park, J. W., Campbell, I. H., Chiaradia, M., Hao, H. & Lee, C. T. Crustal magmatic controls on the formation of porphyry copper deposits. *Nat. Rev. Earth Environ.* **2**, 542–557 (2021).
54. Park, J. W. & Campbell, I. Platinum-group element geochemistry of the volcanic rocks associated with the Jaguar and Bentley Cu–Zn volcanogenic massive sulfide (VMS) deposits, Western Australia: implications for the role of chalcophile element fertility on VMS mineralization. *Mineralium Depos.* **56**, 583–600 (2021).
55. Zhang, Y. Toward a quantitative model for the formation of gravitational magmatic sulfide deposits. *Chem. Geol.* **391**, 56–73 (2015).
56. Turner, S. & Costa, F. Measuring timescales of magmatic evolution. *Elements* **3**, 267–272 (2007).
57. Behrens, H. & Gaillard, F. Geochemical aspects of melts: volatiles and redox behavior. *Elements* **2**, 275–280 (2006).
58. Larocque, A. C., Stimac, J. A., Keith, J. D. & Huminicki, M. A. Evidence for open-system behavior in immiscible Fe–S–O liquids in silicate magmas: implications for contributions of metals and sulfur to ore-forming fluids. *Can. Mineralogist* **38**, 1233–1249 (2000).
59. Costa, F., Shea, T. & Ubide, T. Diffusion chronometry and the timescales of magmatic processes. *Nat. Rev. Earth Environ.* **1**, 201–214 (2020).
60. Williams, T. J., Candela, P. A. & Piccoli, P. M. The partitioning of copper between silicate melts and two-phase aqueous fluids: an experimental investigation at 1 kbar, 800 C and 0.5 kbar, 850 C. *Contrib. Mineral. Petrol.* **121**, 388–399 (1995).
61. Simon, A. C., Pettke, T., Candela, P. A., Piccoli, P. M. & Heinrich, C. A. Copper partitioning in a melt–vapor–brine–magnetite–pyrrhotite assemblage. *Geochim. Cosmochim. Acta* **70**, 5583–5600 (2006).
62. Phillips, G. N. & Evans, K. A. Role of CO₂ in the formation of gold deposits. *Nature* **429**, 860–863 (2004).
63. Kim, J. et al. Venting sites along the Fonualei and Northeast Lau Spreading Centers and evidence of hydrothermal activity at an off-axis caldera in the northeastern Lau Basin. *Geochem. J.* **43**, 1–13 (2009).
64. Richards, J. P. The oxidation state, and sulfur and Cu contents of arc magmas: implications for metallogeny. *Lithos* **233**, 27–45 (2015).
65. Scaillet, B. & Macdonald, R. Experimental and thermodynamic constraints on the sulphur yield of peralkaline and metaluminous silicic flood eruptions. *J. Petrol.* **47**, 1413–1437 (2006).
66. Park, J. W., Campbell, I. H. & Kim, J. Abundances of platinum group elements in native sulfur condensates from the Niuatahi-Motutahi submarine volcano, Tonga rear arc: Implications for PGE mineralization in porphyry deposits. *Geochim. Cosmochim. Acta* **174**, 236–246 (2016).
67. Freda, C., Baker, D. R. & Scarlato, P. Sulfur diffusion in basaltic melts. *Geochim. Cosmochim. Acta* **69**, 5061–5069 (2005).
68. Giordano, D., Russell, J. K. & Dingwell, D. B. Viscosity of magmatic liquids: a model. *Earth Planet. Sci. Lett.* **271**, 123–134 (2008).
69. Marsh, B. D. Magma chambers. *Annu. Rev. Earth Planet. Sci.* **17**, 439–472 (1989).
70. Pearce, N. J. et al. A compilation of new and published major and trace element data for NIST SRM 610 and NIST SRM 612 glass reference materials. *Geostand. Newsl.* **21**, 115–144 (1997).
71. Gao, S. et al. Determination of forty-two major and trace elements in USGS and NIST SRM glasses by laser ablation-inductively coupled plasma-mass spectrometry. *Geostand. Newsl.* **26**, 181–196 (2002).
72. Jochum, K. P. et al. Determination of reference values for NIST SRM 610–617 glasses following ISO guidelines. *Geostand. Geoanalytical Res.* **35**, 397–429 (2011).
73. Park, J. W., Campbell, I. H. & Eggins, S. M. Enrichment of Rh, Ru, Ir and Os in Cr spinels from oxidized magmas: evidence from the Ambae volcano, Vanuatu. *Geochim. Cosmochim. Acta* **78**, 28–50 (2012).
74. Meisel, T. & Moser, J. Platinum-group element and rhenium concentrations in low abundance reference materials. *Geostand. Geoanalytical Res.* **28**, 233–250 (2004).
75. Bézou, A., Guivel, C., La, C., Fougereux, T. & Humler, E. Unraveling the confusion over the iron oxidation state in MORB glasses. *Geochim. Cosmochim. Acta* **293**, 28–39 (2021).
76. Jenner, F. E., & O'Neill, H. S. C. Analysis of 60 elements in 616 ocean floor basaltic glasses. *Geochem. Geophys. Geosyst.* **13**, Q02005 (2012).

Acknowledgements

Rocks described in this work were sampled during the FUTUNA2 (2011) and FUTUNA3 (2012) cruises financed through a public-private consortium of Ifremer and industrial groups including Technip, Eramet, and Orano. It was further supported by the Brain Pool (2021H1D3A2A01100043), Mid-Career Researcher (2022R1A2C1011741), and Science Research Center (2022R1A5A1085103) programs through the National Research Foundation (NRF) funded by the Ministry of Science of South Korea and ICT. We thank Captains J.-R. Gléhen and R. Pichard, officers, crew, and co-scientific staff of the oceanographic R.V. *L'Atalante* and H.O.V. Nautile for their professionalism and enthusiasm during the cruises FUTUNA2 and FUTUNA3. We thank J.-P. Oldra for sample preparation, S. Cheron and J. Etoubleau for conducting XRF analyses of Cu and Zn, J. Langlade, M.-L. Rouget, B. Gueguen, and C. La for their assistance in chemical data acquisition, and Alison Chalm, whose native language is English, for reviewing our manuscript. We thank Zhuosen Yao and Youxue Zhang for their help to conduct physical modeling of sulfide growth. We thank Adam Simon and an anonymous reviewer for their helpful and constructive comments and the board of Communications Earth and Environment for their editorial handling.

Author contributions

Funding acquisition was carried out by Y.F., E.P., and G.C (France) and by J.W.P. and A.J. (South Korea). EPMA, LA-ICPMS, and SEM analyses were carried out by A.J., Pd analysis was conducted by A.J. under the supervision of J.H., measurement of the ferric over total iron ratio was performed by A.B. The numerical models were constructed by A.J. The original draft was written by A.J. Conceptualization of the paper was supervised by J.W.P., E.P. and G.C. The draft was reviewed before submission by J.W.P., A.B., E.P., G.C, and J.H.

Competing interests

The authors declare no competing interests.

Additional information

Supplementary information The online version contains supplementary material available at <https://doi.org/10.1038/s43247-024-01571-9>.

Correspondence and requests for materials should be addressed to Aurélien Jeanvoine.

Peer review information *Communications Earth & Environment* thanks Stephen Barnes and Adam Simon for their contribution to the peer review of this work. Primary Handling Editor: Carolina Ortiz Guerrero. A peer review file is available.

Reprints and permissions information is available at <http://www.nature.com/reprints>

Publisher's note Springer Nature remains neutral with regard to jurisdictional claims in published maps and institutional affiliations.

Open Access This article is licensed under a Creative Commons Attribution-NonCommercial-NoDerivatives 4.0 International License, which permits any non-commercial use, sharing, distribution and reproduction in any medium or format, as long as you give appropriate credit to the original author(s) and the source, provide a link to the Creative Commons licence, and indicate if you modified the licensed material. You do not have permission under this licence to share adapted material derived from this article or parts of it. The images or other third party material in this article are included in the article's Creative Commons licence, unless indicated otherwise in a credit line to the material. If material is not included in the article's Creative Commons licence and your intended use is not permitted by statutory regulation or exceeds the permitted use, you will need to obtain permission directly from the copyright holder. To view a copy of this licence, visit <http://creativecommons.org/licenses/by-nc-nd/4.0/>.

© The Author(s) 2024